



Research paper

Multiscale modeling of coupled thermo-hydro-mechanical behavior in ice-bonded granular media subject to freeze-thaw cycles

Jidu Yu ^a, Jidong Zhao ^{a,b,*}, Weijian Liang ^c, Shiwei Zhao ^a

^a Department of Civil and Environmental Engineering, Hong Kong University of Science and Technology, Kowloon, Hong Kong, China

^b HKUST Shenzhen-Hong Kong Collaborative Innovation Research Institute, Shenzhen 518045, China

^c Department of Civil and Environmental Engineering, Hong Kong Polytechnic University, Kowloon, Hong Kong, China

ARTICLE INFO

Keywords:

Frozen soil
Climate warming
Freeze-thaw cycles
Phase transition
Ice bonding effect
THM coupling
Multiscale modeling
Multiphysics modeling
Material point method
Discrete element method

ABSTRACT

We present a novel multiscale framework that integrates the single-point multiphase material point method (MPM) and the discrete element method (DEM) to model the complex freeze-thaw behavior of ice-bonded granular media. The proposed numerical framework is featured by (a) employing the continuum-based MPM to solve the macroscopic governing equations for granular systems involving thermo-hydro-mechanical (THM) coupling and phase transitions, and (b) using the grain-scale discontinuum-based DEM to capture the thermodynamically sensitive mechanical behaviors of ice-bonded granular media. The multiscale framework is constructed by attaching a DEM-based representative volume element (RVE) at each material point in MPM. This RVE serves as a live sample of each material point to track the state-dependent effective stress with respect to the local deformation and thermodynamic conditions like ice saturation, bridging the macroscopic phenomena and the underlying microstructural evolution. In particular, we implement a semi-implicit staggered integration scheme for the macroscale THM-coupled MPM to boost computational efficiency and enhance numerical stability. We also propose an innovative ice saturation-dependent bond contact to effectively reproduce the thermodynamically sensitive mechanical behaviors. The new multiscale framework is first benchmarked against analytical solutions for 1D non-isothermal consolidation problems. We then demonstrate its exceptional capability in simulating intricate freeze-thaw behavior of granular media through a boundary value problem involving cyclic freeze-thaw actions. Further cross-scale analyses reveal its potential in capturing key loading- and state-dependent THM responses with explainable microstructural mechanisms during complex freezing and thawing loading conditions.

1. Introduction

Permafrosts and seasonally frost regions cover almost half of the northern hemisphere's land surface (Evans and Ge, 2017). Ground soils in these regions experience cyclic freezing and thawing due to periodic temperature change. Normal freeze-thaw cycles keep the thawing/freezing depths and the magnitude of frost heave or thaw settlement within a relatively controllable range, providing valuable reference information for engineering designs in cold regions (Andersland and Ladanyi, 2004; Zhang et al., 2008). However, global warming is disrupting regular freeze-thaw dynamics (Schuur et al., 2015; Turetsky et al., 2019; Lewkowitz and Way, 2019; Wang et al., 2020; Ting et al., 2022), resulting in previously constructed civil infrastructure unsafe and requiring re-design soil structures to withstand future thermal regime changes. Climate warming also increases the susceptibility to warming-driven geohazards, such as thaw-induced ground collapse and

retrogressive thaw slump, which poses new risks to nearby infrastructure (Costard et al., 2021; Armstrong et al., 2018; Wang et al., 2016; Niu et al., 2016; Liew et al., 2022; Hjort et al., 2022; Luo et al., 2022). Therefore, it is crucial to comprehensively and accurately predict the freeze-thaw behavior of ice-rich soils under evolving thermal regimes to ensure the secure design and operation of infrastructure in cold regions. This prediction is also instructive for effectively employing ground improvement technologies in cold regions, such as artificial ground freezing technology and thermal pile foundations (Yang et al., 2010; Tounsi et al., 2019; Liu et al., 2022).

Frozen soils, including permafrost and seasonally frozen soils, consist of soil aggregates, ice crystals, and unfrozen water (and air for unsaturated frozen soils). The ice content variation, particularly for seasonally frozen soils, causes significant changes in soil properties during the transition from frozen to unfrozen zones. For ice-rich frozen

* Corresponding author at: Department of Civil and Environmental Engineering, Hong Kong University of Science and Technology, Kowloon, Hong Kong, China.
E-mail addresses: jyubu@connect.ust.hk (J. Yu), jzhao@ust.hk (J. Zhao), wliangab@connect.ust.hk (W. Liang), ceswzhao@ust.hk (S. Zhao).

soils, the presence of pore ice largely blocks the seepage channel of unfrozen water, rendering the porous media almost impermeable. However, the bonding effect of ice helps to improve the soil's stiffness and strength (Lai et al., 2013; Wang et al., 2024). The melting of ice in soils results in a rapid rise in water content and a significant reduction in soil's bearing capacity, which can cause soil structures to become unstable and even exhibit fluid-like properties (Harris et al., 2008). Evidently, the mechanical properties and failure patterns of frozen soils are highly sensitive to thermodynamic conditions, making the constitutive modeling of such materials highly challenging. Additionally, the inherent complexities associated with multiphysics and multiphase interactions, phase transitions, and large deformations in frozen soils further complicate the problems, making the modeling of the freeze-thaw behavior of frozen soils an unresolved issue.

Frozen soils have often been considered granular materials and modeled using two categories of methods, continuum-based methods (e.g., FEM and MPM) and discrete-based methods (e.g., DEM). Continuum-based methods treat frozen soil as a macroscopic continuum described by partial differential equations (PDEs), allowing for simultaneous modeling of multiphysics processes including heat transfer, fluid flow, and mechanical deformation in frozen granular systems (Neaupane et al., 1999; Nishimura et al., 2009; Zhang et al., 2015; Na and Sun, 2017; Shastri et al., 2021; Arzanfudi and Al-Khoury, 2018). However, constitutive models used for modeling frozen soils within the continuum approach framework are often modified from unfrozen soils, introducing quite some phenomenological parameters that are difficult to calibrate or understand. While some recently developed models account for the multiscale features of frozen soils, such as the ice cementation effect and bond breakage (Zhang et al., 2017; Wang et al., 2024), these models can become so complicated as to limit their practical use. Discrete-based methods, represented by DEM, can naturally consider the multiscale nature of granular materials. DEM considers granular materials as assemblies of discrete particles that interact with each other through interparticle forces. It can capture the effect of fabric structure (Wu et al., 2020), particle shape (Liang et al., 2021b; Yu et al., 2020), particle size distribution (Shen et al., 2021), interparticle bond (Zhao et al., 2022b), bond breakage (Zhu et al., 2021; Chang et al., 2023), and other microscopic characteristics without relying on complex phenomenological assumptions. While DEM can effectively consider the discrete nature of frozen soils at the particulate scale, it may not be practical for engineering-scale multiphysics coupling problems.

In computational geomechanics, the hierarchical multiscale modeling approach has become increasingly popular over the past decade (Guo and Zhao, 2014; Wu et al., 2018a; Liang and Zhao, 2019; Zhao et al., 2020). This approach involves using continuum-based methods to solve a boundary value problem at the macroscale level while employing grain-based DEM to compute the material response from a representative volume element (RVE) at each integration point. This approach can both capture the discrete feature of granular materials and consider the multiphysics processes in macroscopic governing equations (Guo and Zhao, 2016; Zhao et al., 2020; Liang et al., 2023). Two representative multiscale approaches are coupled FEM-DEM (Guo and Zhao, 2014; Wu et al., 2018a; Zhao et al., 2020) and coupled MPM-DEM (Liang and Zhao, 2019), with MPM being particularly suitable for simulating practical problems involving large displacements and rotations, such as landslides (Liang and Zhao, 2019; Zhao et al., 2022a), footing penetration (Liang et al., 2021b), and anchor pullout (Liang et al., 2021a). These advantages make the MPM-DEM coupling scheme potentially useful for simulating the multiphase, multiphysics, and multiscale behaviors in freezing and thawing granular media.

This study aims to develop a THM-coupled MPM-DEM to simulate the phase transition and large strain behaviors of granular media subjected to freezing and thawing. The overall strategy for multiscale and multiphysics modeling of freezing and thawing granular media is illustrated in Fig. 1. The single-point, three-phase MPM will be

used to simulate the macroscopic THM and phase transition behaviors of freezing and thawing granular media. Each material point will be embedded with a discrete element representing an assembly of ice-bonded soils. A thermodynamically sensitive bond contact DEM model will be incorporated in each RVE to represent the bonding effect of ice bonds in the frozen soil. The semi-implicit time integration scheme will be used for the MPM solver, allowing large time steps to render better efficiency of DEM computations compared to explicit solvers. Cross-scale analyses will be performed to show the efficacy of the proposed method. The newly developed THM-coupled MPM-DEM can be used not only for modeling frozen soils but also for other granular materials in the presence of ice-like bonds, such as methane hydrate-bearing sediments.

The paper will be organized as follows. Section 2 presents the THM-coupled governing equations for freezing and thawing granular media. The MPM algorithm for solving the macroscopic equations is shown in Section 3. Section 4 presents the discrete element model for ice-bonded soils. The implementation of the MPM-DEM coupling strategy is presented in Section 5. Sections 6 and 7 give some numerical benchmarks and examples. Conclusions are drawn in Section 8.

2. Mathematical model for freezing and thawing granular media

2.1. RVE homogenization and basic assumptions

We consider a saturated, granular material consisting of a uniformly distributed triphasic mixture of solid grains (s), ice crystals (c), and liquid water (l) (Sweidan et al., 2020). The governing equations for the granular media subjected to freezing and thawing are formulated within the framework of single-point multiphase MPM based on the mixture theory (Lewis and Schrefler, 1998; Ehlers, 2002). The local composition of the triphasic continuum is described by volume fraction, denoted as n_π , which represents the volume of π phase over the total volume of a representative volume element (RVE). The contents of ice or unfrozen water in a partially frozen porous media are characterized by the degree of ice saturation S_c or unfrozen water saturation S_l , equaling the ratio of ice or liquid volume fraction to the porosity (Lewis and Schrefler, 1998). Important definitions are summarized as,

$$n_\pi = \frac{dV_\pi}{dV}, \quad \pi \in \{s, c, l\}, \quad \text{and} \quad S_\alpha = \frac{n_\alpha}{\phi}, \quad \alpha \in \{c, l\} \quad (1)$$

where dV_π and dV are the partial and total volume, respectively, and ϕ is the porosity.

To facilitate the establishment of associated mathematical model, we have made the following assumptions.

- During the freeze-thaw process, the phase change occurs only between the ice phase and liquid phase under specific thermodynamic conditions. No other phase, such as the gas phase, is generated or involved in the considered process. No phase change or mass transfer is involved between the solid grains and other phases either.
- Although the occurrence of ice in soil can be diversified, the model considers only the cemented ice between soil particles. The bonded ice is assumed to act as part of the solid skeleton and share effective stress with the soil grains. Therefore, it is natural to neglect the relative velocity between ice and solid grains, i.e., $v_c = v_s$. Moreover, Terzaghi's effective stress theory is assumed to be valid.
- The flow of liquid in both unfrozen and partially frozen soils is in a laminar state, fulfilling Darcy's law. The liquid phase can be either incompressible or weakly compressible, while the compressibility of soil grains and ice is neglected.
- The RVE is assumed to be isothermal, such that no temperature separation between phases is considered in one material point. Only conductive and convective heat transfer are considered, while other heat transfer mechanisms, such as thermal radiation, are not. The heat conduction follows Fourier's law.

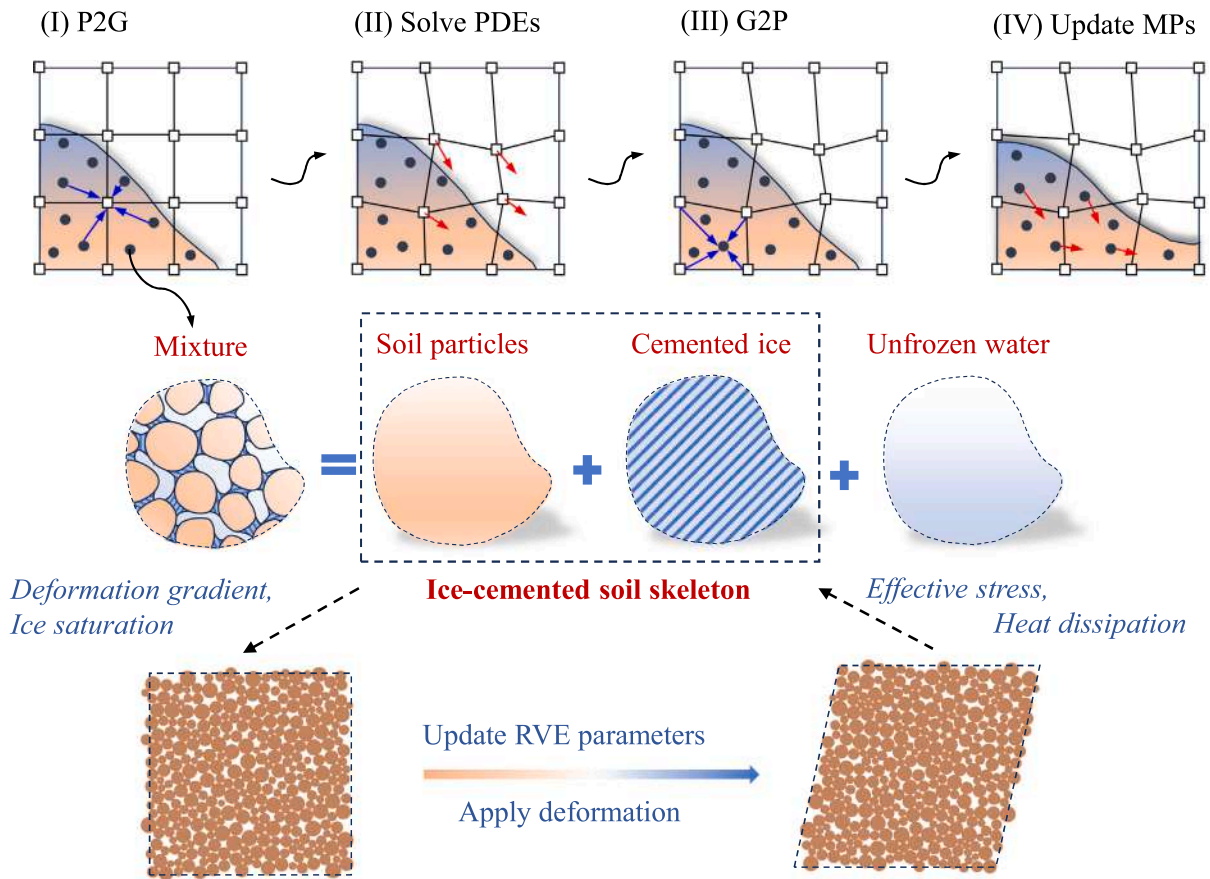


Fig. 1. Overall strategy for multiscale, multiphysics modeling of freezing and thawing granular media.

2.2. Governing equations

2.2.1. Conservation of mass

The mass balance equation is derived based on the conservation of mass of each phase in the Lagrangian description and the non-isothermal state equations that link the intrinsic density of each phase with the thermodynamic properties (Lewis and Schrefler, 1998). Combining all these equations into one yields the final mass balance equation of the mixture,

$$\zeta \phi \frac{D_s S_l}{Dt} + \frac{n_l}{K_l} \frac{D_s p_l}{Dt} - \beta_m \frac{D_s T}{Dt} + (1 - \zeta n_c) \nabla \cdot \mathbf{v}_s + \nabla \cdot n_l (\mathbf{v}_l - \mathbf{v}_s) = 0 \quad (2)$$

where $D_s (*)/Dt$ denotes the material derivative of variable (*) with respect to the solid phase; n_π , ρ_π , β_π , and \mathbf{v}_π are the volume fraction, intrinsic density, thermal expansivity, and velocity of π phase, respectively; $\zeta = 1 - \rho_c/\rho_l$ is the volumetric expansion coefficient of pore water on freezing; $\beta_m = n_s \beta_s + n_l \beta_l + (1 - \zeta) n_c \beta_c$ is the thermal expansivity of the mixture; S_l is the degree of liquid saturation; K_l is the liquid bulk modulus; p_l is the pore liquid pressure; and T is the temperature. The term $\zeta \phi \frac{D_s S_l}{Dt}$ represents the effect of volume expansion/contraction due to ice-water phase transition. To link the liquid saturation with the thermodynamic properties, the following soil freezing characteristic curve (SFCC) modified from van Genuchten model is adopted in this study (van Genuchten, 1980; Nishimura et al., 2009),

$$S_l = \left[1 + \left(-\frac{\rho_c}{P_0} L_f \ln \frac{T + 273.15}{273.15} \right)^{\frac{1}{1-\lambda}} \right]^{-\lambda} \quad (3)$$

where L_f is the latent heat of fusion of ice, and P_0 and λ are two material constants, taken as 100 kPa and 0.4, respectively, in this study. Considering that S_l is dependent only on the temperature in this SFCC model, the derivative of S_l can be expanded as $\frac{D_s S_l}{Dt} = \frac{\partial S_l}{\partial T} \frac{D_s T}{Dt}$.

2.2.2. Conservation of momentum

Based on Assumption (b), two kinematic unknowns remain, i.e., \mathbf{v}_s and \mathbf{v}_l , which requires two independent equations. The following momentum balance equations for the mixture and the liquid phase are adopted,

$$(n_s \rho_s + n_c \rho_c) \frac{D_s \mathbf{v}_s}{Dt} + n_l \rho_l \frac{D_s \mathbf{v}_l}{Dt} = \nabla \cdot (\boldsymbol{\sigma}'_{\text{RVE}} - p_l \mathbf{I}) + \rho_m \mathbf{b} \quad (4)$$

$$n_l \rho_l \frac{D_s \mathbf{v}_l}{Dt} = -n_l \nabla p_l + n_l \rho_l \mathbf{b} - n_l^2 \frac{\rho_l g}{k_a k_r} (\mathbf{v}_l - \mathbf{v}_s) \quad (5)$$

where $\boldsymbol{\sigma} = \boldsymbol{\sigma}'_{\text{RVE}} - p_l \mathbf{I}$ is the total stress; $\boldsymbol{\sigma}'_{\text{RVE}}$ is the effective stress for ice-bonded solid skeleton (which will be obtained from the RVE attached on each MP); \mathbf{I} is the identity tensor; \mathbf{b} is the body force vector; $\rho_m = n_s \rho_s + n_c \rho_c + n_l \rho_l$ is the mixture density; k_a is the absolute hydraulic conductivity; k_r is the relative hydraulic conductivity; and g is the gravitational acceleration. k_r is highly dependent on the S_l , and the following expression (Nishimura et al., 2009) is adopted,

$$k_r = \sqrt{S_l} \left[1 - (1 - S_l^{1/\lambda})^\lambda \right]^2 \quad (6)$$

It is important to note that the presented model does not explicitly consider the pore ice pressure in the stress decomposition. Experimental studies on soil freezing often observe suctions or negative pore pressure that supplies water, promoting ice crystal growth in freezing fringes (Eigenbrod et al., 1996; Zhang et al., 2015). To replicate the suction effect, previous works (Nishimura et al., 2009; Sweidan et al., 2020; Suh and Sun, 2022) have introduced the pore ice pressure p_c as an independent state variable. The determination of p_c is typically based on the thermodynamically consistent Clausius–Clapeyron (C–C) equation. However, it has been found that p_c calculated from the C–C equation is often overestimated and not consistent with the experimental observations. This is likely due to the fact that the C–C

equation is only valid under equilibrium or static conditions, while soil freezing and thawing may tend to be a non-equilibrium (irreversible) thermodynamic process (Kurylyk and Watanabe, 2013; Ma et al., 2015). In our model, the ice phase is considered part of the solid skeleton, which means that the resulting effective stress incorporates both the mechanical responses of soil particles and ice particles. In other words, the ice pressure is implicitly integrated into the effective stress. The stress–strain relations of the ice-enhanced solid skeleton will be captured by a bond-contact DEM model, and the cryogenic suction can also be considered a type of bond. Therefore, there is no need to explicitly consider pore ice pressure and cryogenic suction in the governing equations. With this approach, we can successfully replicate the negative pore water pressure and the evolution of pore water pressure observed in experiments, as demonstrated later in Section 7.

2.2.3. Conservation of energy

Based on Assumption (d), the energy balance equation for the triphasic mixture involving water-ice phase transition can be written into one single equation as follows,

$$C_m \frac{D_s T}{Dt} + \rho_c L_f \phi \frac{D_s S_l}{Dt} + n_l \rho_l c_l (\mathbf{v}_l - \mathbf{v}_s) \cdot \nabla T + \nabla \cdot (-\kappa_m \nabla T) = Q \quad (7)$$

where $C_m = n_s \rho_s c_s + n_l \rho_l c_l + n_c \rho_c c_c$ is the matrix heat capacity; c_π is the specific heat capacity of π phase; L_f is the latent heat of fusion of ice; $\kappa_m = n_s \kappa_s + n_l \kappa_l + n_c \kappa_c$ is the thermal conductivity of mixture; κ_π is the thermal conductivity of π phase; and Q is the heat source. The term $\rho_c L_f \phi \frac{D_s S_l}{Dt}$ represents the latent heat effect during the ice-liquid phase transition. Note that plastic heat generation as one of the heat sources can be extracted from the RVE through particle-based DEM modeling (Zhao et al., 2022b).

2.2.4. Boundary conditions

The material domain is denoted by Ω with its boundary denoted by $\partial\Omega$. For THM-coupled problems, the boundary conditions are given as follows,

$$\mathbf{v}_\alpha = \hat{\mathbf{v}}_\alpha \text{ on } \partial\Omega_{v_\alpha} \quad (8)$$

$$p_l = \hat{p}_l \text{ on } \partial\Omega_p \quad (9)$$

$$T = \hat{T} \text{ on } \partial\Omega_T \quad (10)$$

$$\mathbf{n} \cdot \boldsymbol{\sigma} = \hat{\mathbf{t}} \text{ on } \partial\Omega_t \quad (11)$$

$$\mathbf{n} \cdot (-n_l p_l \mathbf{I}) = \hat{\mathbf{t}}_l \text{ on } \partial\Omega_{t_l} \quad (12)$$

$$-\mathbf{n} \cdot \mathbf{q} = \hat{q} \text{ on } \partial\Omega_q \quad (13)$$

where $\hat{\mathbf{v}}_\alpha$, \hat{p}_l , \hat{T} , $\hat{\mathbf{t}}_l$ and \hat{q} are the specified velocity, pore pressure, temperature, mixture traction, liquid traction, and heat flux respectively, and \mathbf{n} is the outward unit surface normal.

3. Semi-implicit MPM for macroscale multiphysics modeling

3.1. Semi-implicit time integration

Despite being a popular scheme, the explicit integration is subject to the restriction of small timestep when considering nearly incompressible interstitial fluid and the potential low permeability in frozen soils (Kurylyk and Watanabe, 2013). It is not suitable for the current multiscale, multiphysics approach since it will inevitably cause persistent message passing overhead between MPM and DEM solver and significantly deteriorate the overall computational efficiency. Therefore, we resort to the semi-implicit scheme proposed previously by the authors (Yu et al., 2024a,b) for the present MPM solver. Central to the scheme is the use of implicit integration for the pore pressure and the drag force term to eliminate the constraint of liquid compressibility and permeability on the global timestep size while using explicit integration for the stress term and temperature field to avoid massive matrix assembly and iterative solutions. Additionally, the simultaneous

solutions of pore pressure and kinematic unknowns may suffer spurious pressure oscillations when using equal-order interpolation. The interpolation restriction is further eliminated by employing a fractional step scheme (Kularathna et al., 2021; Yuan et al., 2022, 2023). The key point of the scheme is decomposing the momentum Eqs. (4) and (5) into a predicting part and a correcting part via intermediate velocities, \mathbf{v}_s^* and \mathbf{v}_l^* , thereby decoupling the pressure fields and velocity fields. Consequently, the primary unknowns can be solved sequentially according to the following temporally discretized governing equations:

(1) Compute the temperature T explicitly based on the energy Eq. (7),

$$\left(C_m + \rho_c L_f \phi \frac{\partial S_l}{\partial T} \right) \frac{T^{k+1} - T^k}{\Delta t} + n_l \rho_l c_l (\mathbf{v}_l^k - \mathbf{v}_s^k) \cdot \nabla T^k + \nabla \cdot (-\kappa_m \nabla T^k) = Q \quad (14)$$

(2) Compute the intermediate velocities \mathbf{v}_s^* and \mathbf{v}_l^* based on the predicting part of momentum balance equations,

$$(n_s \rho_s + n_c \rho_c) \frac{\mathbf{v}_s^* - \mathbf{v}_s^k}{\Delta t} + n_l \rho_l \frac{\mathbf{v}_l^* - \mathbf{v}_l^k}{\Delta t} = \nabla \cdot (\boldsymbol{\sigma}_{\text{RVE}}^k - p_l^k \mathbf{I}) + \rho_m \mathbf{b} \quad (15)$$

$$n_l \rho_l \frac{\mathbf{v}_l^* - \mathbf{v}_l^k}{\Delta t} = -n_l \nabla p_l^k + n_l \rho_l \mathbf{b} - n_l^2 \frac{\rho_l g}{k_a k_r} (\mathbf{v}_l^* - \mathbf{v}_s^*) \quad (16)$$

(3) Compute the pore pressure p_l from the pressure Poisson equation obtained by substituting the separated \mathbf{v}_s^{k+1} and \mathbf{v}_l^{k+1} from Eqs. (18) and (19) into the mass balance Eq. (2),

$$\Delta t \left[\frac{n_l}{\rho_l} + (n_s + n_c - \zeta n_c) \frac{n_s + n_c}{n_s \rho_s + n_c \rho_c} \right] \nabla^2 (p_l^{k+1} - p_l^k) - \frac{n_l}{K_l} \frac{p_l^{k+1} - p_l^k}{\Delta t} - \left(\zeta \phi \frac{\partial S_l}{\partial T} - \beta_m \right) \frac{T^{k+1} - T^k}{\Delta t} = (1 - \zeta n_c) \nabla \cdot \mathbf{v}_s^* + \nabla \cdot n_l (\mathbf{v}_l^* - \mathbf{v}_s^*) \quad (17)$$

(4) Compute the end-of-step velocities \mathbf{v}_s^{k+1} and \mathbf{v}_l^{k+1} based on the correcting part of momentum balance equations,

$$(n_s \rho_s + n_c \rho_c) \frac{\mathbf{v}_s^{k+1} - \mathbf{v}_s^*}{\Delta t} = -(n_s + n_c) \nabla (p_l^{k+1} - p_l^k) \quad (18)$$

$$n_l \rho_l \frac{\mathbf{v}_l^{k+1} - \mathbf{v}_l^*}{\Delta t} = -n_l \nabla (p_l^{k+1} - p_l^k) \quad (19)$$

Since the scheme is not fully implicit, the timestep size is still constrained by the rate of p-wave propagation and heat diffusion (Kularathna et al., 2021; Yuan et al., 2023; Zhao et al., 2022b). The critical time step size is estimated as follows,

$$\Delta t < \min \left\{ L_{\min}^2 \frac{C_m}{\kappa_m}, L_{\min} \sqrt{\frac{n_s \rho_s + n_c \rho_c}{M_{sc}}} \right\} \quad (20)$$

where L_{\min} is the minimum element size and M_{sc} is the p -wave modulus of ice-bonded soil. Note that the value of n_c and M_{sc} may vary significantly during ice freezing and thawing, we estimate the least favorable conditions, namely, when the pore space is fully filled by ice.

3.2. MPM discretization

Before proceeding to the MPM discretization, the semi-discrete equations are written into weak form by introducing test functions. Then, the spatial discretization of the weak equations is performed based on the standard GIMP method. The typical feature of GIMP is to describe the physical properties of material points with weighting function S_{ip} and gradient weighting functions ∇S_{ip} , with

$$S_{ip} = \frac{1}{V_p} \int_{\Omega_p \cap \Omega} \chi_p(\mathbf{x}) N_i(\mathbf{x}) dV, \quad \nabla S_{ip} = \frac{1}{V_p} \int_{\Omega_p \cap \Omega} \chi_p(\mathbf{x}) \nabla N_i(\mathbf{x}) dV \quad (21)$$

where Ω and Ω_p represent the material domain and the subdomain occupied by each material point, respectively; N_i is the grid shape function; χ_p is the particle characteristic function; and $V_p = \int_{\Omega_p} \chi_p(\mathbf{x}) dV$ is the volume of material point p .

With the weighing functions, the governing equations can be discretized into the following summation forms.

(1) Energy balance equation:

$$\mathcal{M}_T \dot{\mathcal{T}}^{k+1} - f_T = \mathbf{0} \quad (22)$$

with

$$\mathcal{M}_T = \int_{\Omega} \mathbf{S}^T \left(C_m + \rho_c L_f \phi \frac{\partial S_l}{\partial T} \right) S dV \quad (23)$$

$$f_T = - \int_{\Omega} \mathbf{S}^T n_l \rho_l c_l (\mathbf{v}_l^k - \mathbf{v}_s^k) \nabla T dV + \int_{\partial \Omega_q} \mathbf{S}^T \hat{q} dS - \int_{\Omega} \nabla \mathbf{S}^T \kappa_m \nabla T dV + \int_{\Omega} \mathbf{S}^T Q dV \quad (24)$$

(2) Momentum balance equations — predicting part:

$$\mathcal{M}_{11} \dot{\mathbf{v}}_s^* + \mathcal{M}_{12} \dot{\mathbf{v}}_i^* - f_1 = \mathbf{0} \quad (25)$$

$$\mathcal{M}_{22} \dot{\mathbf{v}}_i^* + \mathcal{K}_{21} \mathbf{v}_s^* + \mathcal{K}_{22} \mathbf{v}_i^* - f_2 = \mathbf{0} \quad (26)$$

with

$$\mathcal{M}_{11} = \int_{\Omega} \mathbf{S}^T (n_s \rho_s + n_c \rho_c) S dV \quad (27)$$

$$\mathcal{M}_{12} = \mathcal{M}_{22} = \int_{\Omega} \mathbf{S}^T n_l \rho_l S dV \quad (28)$$

$$\mathcal{K}_{22} = -\mathcal{K}_{21} = \int_{\Omega} \mathbf{S}^T n_l^2 \frac{\rho_l g}{k_d k_r} S dV \quad (29)$$

$$f_1 = \int_{\partial \Omega_i} \mathbf{S}^T \hat{i} dS - \int_{\Omega} \nabla \mathbf{S}^T : \boldsymbol{\sigma}^k dV + \int_{\Omega} \mathbf{S}^T \rho_m b dV \quad (30)$$

$$f_2 = \int_{\partial \Omega_i} \mathbf{S}^T \hat{i}_l dS - \int_{\Omega} \nabla \mathbf{S}^T : (-n_l p_l^k \mathbf{I}) dV + \int_{\Omega} \mathbf{S}^T n_l \rho_l b dV \quad (31)$$

(3) Pressure Poisson equation:

$$\mathcal{M}_{33} \dot{\mathbf{p}}_l^{k+1} + \mathcal{M}_{34} \dot{\mathcal{T}}^{k+1} + \mathcal{K}_{31} \mathbf{v}_s^* + \mathcal{K}_{32} \mathbf{v}_i^* + \mathcal{K}_{33} (\mathbf{p}_l^{k+1} - \mathbf{p}_l^k) = \mathbf{0} \quad (32)$$

with

$$\mathcal{M}_{33} = \int_{\Omega} \mathbf{S}^T \frac{n_l}{K_l} S dV \quad (33)$$

$$\mathcal{M}_{34} = \int_{\Omega} \mathbf{S}^T \left(\zeta \phi \frac{\partial S_l}{\partial T} - \beta_m \right) S dV \quad (34)$$

$$\mathcal{K}_{31} = \int_{\Omega} \mathbf{S}^T (1 - \zeta n_c) \nabla S d\Omega + \int_{\Omega} \nabla \mathbf{S}^T n_l S dV \quad (35)$$

$$\mathcal{K}_{32} = - \int_{\Omega} \nabla \mathbf{S}^T n_l S dV \quad (36)$$

$$\mathcal{K}_{33} = \int_{\Omega} \nabla \mathbf{S}^T \Delta t \left(\frac{n_l}{\rho_l} + (n_s + n_c - \zeta n_c) \frac{n_s + n_c}{n_s \rho_s + n_c \rho_c} \right) \nabla S dV \quad (37)$$

(4) Momentum balance equations — correcting part:

$$\mathcal{M}_{11} (\dot{\mathbf{v}}_s^{k+1} - \dot{\mathbf{v}}_s^*) + \mathcal{K}_{13} (\mathbf{p}_l^{k+1} - \mathbf{p}_l^k) = \mathbf{0} \quad (38)$$

$$\mathcal{M}_{22} (\dot{\mathbf{v}}_i^{k+1} - \dot{\mathbf{v}}_i^*) + \mathcal{K}_{23} (\mathbf{p}_l^{k+1} - \mathbf{p}_l^k) = \mathbf{0} \quad (39)$$

with

$$\mathcal{K}_{13} = \int_{\Omega} \mathbf{S}^T (n_s + n_c) \nabla S dV \quad (40)$$

$$\mathcal{K}_{23} = \int_{\Omega} \mathbf{S}^T n_l \nabla S dV \quad (41)$$

where $\dot{\mathcal{T}}^{k+1}$, $\dot{\mathbf{p}}_l^{k+1}$, $\dot{\mathbf{v}}_s^*$, and $\dot{\mathbf{v}}_i^{k+1}$ are the columns of nodal rate of temperature, pore pressure, intermediate velocity, and end-of-step velocity, respectively.

4. Discrete element model for ice-bonded soils

The bonding effect of ice in frozen soils has been extensively investigated by both laboratory and numerical tests (Xu et al., 2011; Zhou et al., 2018; Xu et al., 2020; Zhu et al., 2021; Chang et al., 2023; Sun et al., 2023). It is found that the strength of frozen soil increases with the increase in ice content and the confining pressure but may

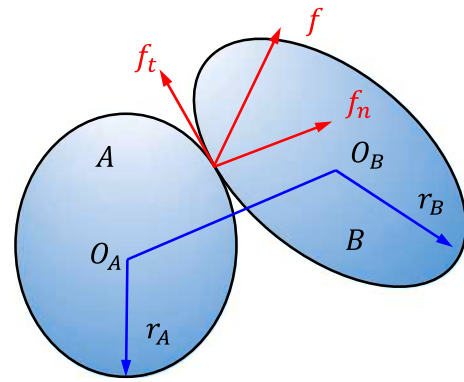


Fig. 2. Illustration of contact model in DEM solver.

decrease with a further increase in confining pressure when the bond between soil particles and ice crystals breaks. Therefore, it is essential to consider the bonding effect in the constitutive modeling of frozen soils under cyclic freeze-thaw loading (Zhang et al., 2017; Zhao et al., 2020; Ma et al., 2022). Instead of using conventional phenomenological constitutive models, a bond contact-based DEM model is employed to generate the stress–strain relationship of soils in frozen and unfrozen states to advance the macroscopic THM responses. DEM has been increasingly used for modeling the micro-macroscopic mechanical behavior of frozen soils (Chang et al., 2023; Zhu et al., 2021; Sun et al., 2023). For simplicity but without generality, we employ a frictional contact model for the basic contact without ice bond (Liang and Zhao, 2019; Liang et al., 2023; Zhao et al., 2022a), and further employ a simple bond contact model to characterize the bonding effect of ice between soil particles (Wu et al., 2018a,b; Zhao et al., 2022a). The approach can naturally consider the following effects: (1) the effect of ice bonding, (2) the effect of ice content on the bond strength and the soil stiffness, (3) ice bond breakage when the grain contact force exceeds the bond strength, (4) bond formation/melting during phase transition, (5) the dependence of soil strength and stiffness on ice content, confined stress, and packing density, (6) path and history-dependent stress–strain relationships during freeze-thaw cycles, and (7) other microscopic properties.

4.1. Basic frictional contact model

The contact forces of each pair of contacting grains, for example, particle A and particle B, as depicted in Fig. 2, are linearly related to the relative displacement as follows,

$$f_n = -k_n u_n \quad (42)$$

$$\Delta f_t = -k_t \Delta u_t \quad (43)$$

and the tangential contact force is constrained by the Coulomb condition of friction according to,

$$|f_t| \leq \mu |f_n| \quad (44)$$

where f_n and f_t are the normal and tangential components of the contact force (with the convention of positive tensile forces); k_n and k_t are the normal and the tangential stiffnesses; u_n and u_t are the normal and tangential displacement; and μ is the friction coefficient at the contact. k_n and k_t are interchangeable with the grains' Young's modulus E_c and Poisson's ratio ν_c through $k_n = E_c \bar{r}$ and $k_t = \nu_c k_n$, where $\bar{r} = 2r_A r_B / (r_A + r_B)$ is the harmonic radius of two contacting particles with radii r_A and r_B .

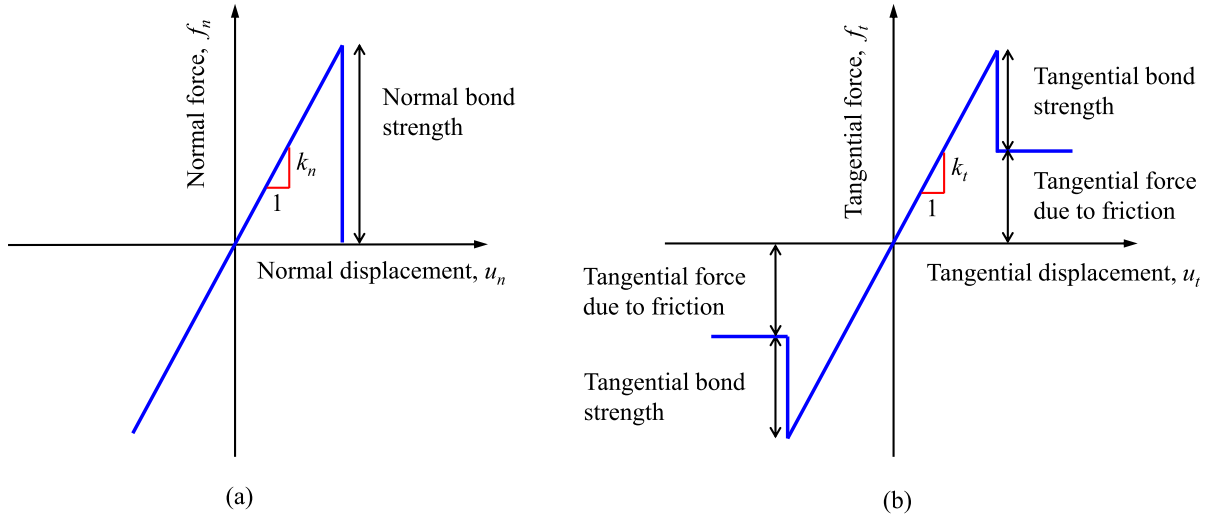


Fig. 3. The relation of contact force and relative particle displacement at a bond contact in (a) normal direction and (b) tangential direction (Wu et al., 2018b).

4.2. Bond contact model for ice-bonded solid skeleton

Since it is challenging to explicitly consider the formation and melting of ice particles in RVE assembly with a limited number of particles, we assume that the ice masses are concentrated at the surrounding soil particles (Zhao et al., 2022a). Accordingly, the equivalent size of the soil-ice mixed particle (2D), r_{eq} , can be estimated as,

$$r_{eq} = r_0 \sqrt{\frac{V_s + V_c}{V_{s0}}} = r_0 \sqrt{\frac{1 - \phi_0 + (\phi_0 + \epsilon_v) S_i}{1 - \phi_0}} \quad (45)$$

where r_0 is the initial grain size; V_{s0} is the initial volume of the solid phase; V_s and V_c are the current volumes of the solid phase and the ice phase, respectively; ϕ_0 is the initial porosity; ϵ_v is the volumetric strain; and S_i is the ice saturation degree.

The relation of particle contact force and relative particle displacement at a bond contact is illustrated in Fig. 3. The maximum normal and tangential contact forces, f_n^{max} and f_t^{max} , are defined as,

$$f_n^{max} = C_n \min \{r_A^2, r_B^2\} \quad (46)$$

$$f_t^{max} = \mu f_n + C_t \min \{r_A^2, r_B^2\} \quad (47)$$

where C_n and C_t are the normal and tangential cohesion strength of the bond. If either the normal or tangential force exceeds its maximum value, the bond will break. If the normal force is in a tensile state, the contact will be lost. Otherwise, the contact will transition to a pure frictional contact.

Considering that the bond strength and the particle stiffness are highly dependent on the ice content (Lai et al., 2013), they are linked with the ice saturation as follows,

$$C_i = C_{i0} + \Delta C_i^{max} \Phi_{ci}(S_c), \quad i = n, t \quad (48)$$

$$k_i = k_{i0} + \Delta k_i^{max} \Phi_{ki}(S_c), \quad i = n, t \quad (49)$$

where C_{i0} and k_{i0} are the cohesion strength and the particle stiffness without ice bond; ΔC_i^{max} and Δk_i^{max} are the maximum additional cohesion and stiffness due to ice bond; and Φ_{ci} and Φ_{ki} are functions related to ice saturation S_c . The stiffness can also be considered in terms of Young's modulus of grains as $E_c = E_{c0} + \Delta E_c^{max} \Phi$, where E_{c0} is the Young's modulus of pure soil grains and ΔE_c^{max} is the maximum additional modulus due to ice presence.

Since the bonding effect might not be significant when ice saturation is low, an S-shaped Φ function is adopted for Φ_{ci} and Φ_{ki} ,

$$\Phi_{ci} = \Phi_{ki} = \Phi = 1 - (1 - S_c^m)^m \quad (50)$$

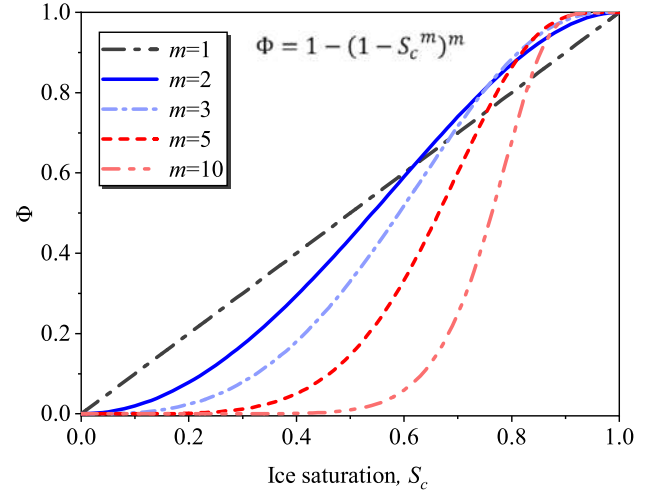


Fig. 4. Φ function with different shape parameter m .

where m is a shape parameter. Fig. 4 illustrates the Φ as a function of m . If the ice saturation S_c is low, the corresponding value of Φ is also small, indicating an insignificant bonding effect. A higher value of m suggests a less pronounced bonding effect under conditions of low ice saturation. Additionally, there may exist another type of bonding effect between soil particles apart from the bonding induced by ice cementation, namely, the cryogenic suction effect (Nishimura et al., 2009; Na and Sun, 2017; Suh and Sun, 2022). Cryogenic suction can be considered an equivalent bond between particles. Indeed, the bonding effect may still be present even when ice saturation is low. For this concern, this study adopts a value of $m = 2$ to generate a relatively small but non-zero bonding effect during the low ice saturation stage. More advanced contact models (e.g., parallel contact bond model, rolling resistance frictional contact model) can also be implemented to consider more detailed mechanisms (e.g., bending, twisting, and rolling) at the particulate level, which is out of the scope of this study.

4.3. Periodic cell, boundary condition, and homogenized stress

An RVE assembly is assumed to be sufficiently small to capture the response of a material point from the macroscopic perspective and, meanwhile, sufficiently large to yield a representative response with respect to discrete grains. To reduce the boundary effect from

rigid boundaries (e.g., rigid confining walls), periodic boundary conditions are employed in the DEM simulations (Liang et al., 2023). In the implementation, the boundary condition of the RVE over time is quantified via a tensor deformation gradient \mathbf{F} , which represents arbitrary combinations of compression, simple shear, and rotations. The incremental displacement gradient $\nabla \mathbf{u}^k$ is received from the macroscale MPM material point to prescribe as boundary conditions of an RVE. For non-isothermal conditions, the displacement gradient in MPM solver is calculated by,

$$\nabla \mathbf{u}^k = \Delta t \nabla \mathbf{v}_s^k - \beta_s \Delta T^k \mathbf{I} \quad (51)$$

in which the second term on the right-hand side denotes the volumetric expansion/contraction due to the thermal effect. Specifically, we first compute the corresponding velocity gradient $\nabla \mathbf{v}^k$ from the downscaled information: $\nabla \mathbf{v}^k = \nabla \mathbf{u}^k / \Delta t_{\text{DEM}}$, with Δt_{DEM} being the time step of DEM solver. This velocity gradient is then integrated automatically over time, and the accumulated transformation is reflected in the transformation matrix \mathbf{F} .

$$\mathbf{F}^{k+1} = \mathbf{I} + \nabla \mathbf{v}^k \Delta t_{\text{DEM}} \mathbf{F}^k \quad (52)$$

The homogenized Cauchy stress is computed based on the well-established Love-Weber formula (Nicot et al., 2013),

$$\boldsymbol{\sigma}'_{\text{RVE}} = \frac{1}{V_{\text{RVE}}} \sum_{N_c} \mathbf{d} \otimes \mathbf{f} \quad (53)$$

where “ \otimes ” denotes the dyadic product between two vectors; V_{RVE} is the volume of the RVE; N_c is the total number of all contacts inside the RVE; \mathbf{d} is the branch vector joining the centers of contacting particles; and \mathbf{f} is the contact force.

The mean effective stress σ_v and the deviatoric stress σ_d (for 2D) are defined as,

$$\sigma_v = \frac{1}{2} \text{tr}(\boldsymbol{\sigma}'_{\text{RVE}}) \quad (54)$$

$$\sigma_d = \sqrt{\frac{1}{2} \mathbf{s} : \mathbf{s}} \quad (55)$$

where “ tr ” indicates the trace of a tensor and $\mathbf{s} = \boldsymbol{\sigma}'_{\text{RVE}} - \sigma_v \mathbf{I}$ is the deviatoric stress tensor. The volumetric and deviatoric strains (scalar), ε_v and ε_d , can be respectively computed according to,

$$\varepsilon_v = \text{tr}(\boldsymbol{\varepsilon}) \quad (56)$$

$$\varepsilon_d = \sqrt{2\mathbf{e} : \mathbf{e}} \quad (57)$$

where $\boldsymbol{\varepsilon}$ is the strain tensor, and $\mathbf{e} = \boldsymbol{\varepsilon} - \varepsilon_v \mathbf{I} / 2$ is the deviatoric strain tensor.

5. Coupled MPM-DEM for hierarchical multiscale modeling

The multiscale framework by MPM and DEM is implemented by attaching an RVE on each material point to update stresses and other properties, as illustrated in Fig. 1. The MPM serves as the macroscale solver to obtain the continuum-level THM response. The deformation and other thermodynamic information computed from the MPM solver, such as temperature, pore pressure, and ice saturation, are transferred to the downscale DEM solver as the boundary conditions. The particle-based DEM solver then returns the homogenized stress and other mesoscale information, such as heat generation and porosity, as feedback to further advance the MPM solver. It is worth noting that the RVE keeps its memory of the previous loading state during each incremental time step. This allows to provide a history-dependent stress feedback which is particularly important for the modeling of time-dependent freeze-thaw behavior of granular soils by bond contact model. The two-way cross-scale message passing is executed for every MPM timestep. Since the scale of time for MPM and DEM solvers is separate and the semi-implicit MPM scheme allows the use of a relatively large timestep, the executive time of the DEM solver could be largely shortened compared to the explicit MPM. Besides, the RVEs

attached to each material are independent, so it is rather convenient to perform parallel computing with multiple CPU or GPU nodes. In this work, we adopt an effective, scalable parallel scheme based on the flat message-passing interface (MPI) model to accelerate the multiscale simulation (Liang et al., 2022). The overall strategy of the coupled MPM-DEM approach is shown in Fig. 5.

6. Numerical benchmarks

The macroscopic MPM solver for simulating the TH and THM responses during water-ice phase transition has been validated in our parallel work (Yu et al., 2024b). Since the multiscale solver for modeling the phase transition process may inevitably involve highly nonlinear responses, which is particularly difficult to benchmark, we here validate the proposed multiscale approach via two simple examples without considering phase transition.

6.1. 1D non-isothermal consolidation

The classical 1D thermoelastic consolidation problem is first revisited to benchmark the multiphysics multiscale solver (Noorishad et al., 1984; Lewis et al., 1986; Cui et al., 2018; Lei et al., 2021). A saturated soil column with a height of $h = 1$ m and an initial temperature of $T_0 = 0$ °C is considered, as illustrated in Fig. 6(a). The bottom side is a fixed boundary, while the vertical sides are roller boundaries. The top surface is subjected to a constant temperature, T_s , and a constant surface surcharge, q_s . The soil material is assumed to be perfectly elastic. The analytical solution for temperature T and pore pressure p at the time t and the depth x is expressed as (Wu, 2008),

$$T(x, t) = T_s \left(1 - \sum_{n=0}^{\infty} \frac{2}{\xi h} \sin \xi x \cdot e^{-\xi^2 \kappa t} \right) \quad (58)$$

$$p(x, t) = \sum_{n=0}^{\infty} \frac{2}{\xi} \sin \xi x \left[\frac{bT_s}{1 - c/\kappa} e^{-\xi^2 \kappa t} + \left(q_s - \frac{bT_s}{1 - c/\kappa} \right) e^{-\xi^2 ct} \right] \quad (59)$$

and the solution of surface displacement u_s is expressed as,

$$u_s(t) = \frac{h}{M} \left[\beta T_s - q_s + \sum_{n=0}^{\infty} \frac{2}{\xi^2 h^2} \left[\left(\frac{bT_s}{1 - c/\kappa} - \beta T_s \right) e^{-\xi^2 \kappa t} + \left(q_s - \frac{bT_s}{1 - c/\kappa} \right) e^{-\xi^2 ct} \right] \right] \quad (60)$$

where $\xi = (2n + 1)\pi / (2h)$, $c = kM / \rho_l g$, $\kappa = \kappa_m / C_m$, $b = \beta - \beta_m M$, $\beta = \beta_s (3\lambda + 2G)$, $\beta_m = n_s \beta_s + n_l \beta_l$, and $M = \lambda + 2G$. In the above, c is the consolidation coefficient, κ is the thermal diffusion coefficient, C_m and κ_m are the heat capacity and heat conductivity of the soil matrix, and λ and G are the Lamé constants. For comparison, three boundary value problems are designed as shown in Fig. 6(a). **Case 1** is a pure HM coupling problem, also known as the Terzaghi 1D consolidation problem, whereas **Case 2** and **Case 3** are two THM coupling problems.

Since the benchmark problem does not involve the phase transition process, the pure frictional contact model will be employed in the RVE for multiscale simulations. The microscopic parameters used for RVE are shown in Table 1. A dense RVE packing is prepared with an isotropic confined stress of 100 kPa and an initial porosity of 0.1647, as shown in Fig. 6(b). To benchmark the multiscale simulations, the RVE's elastic parameters are estimated via the oedometer compression test to the RVE under a small-strain regime wherein particles undergo negligible sliding over each other. As shown in Fig. 6(c), the elastic parameters are estimated as $\lambda + 2G = 23.53$ MPa and $\lambda = 4.41$ MPa. Accordingly, the RVE's Young's modulus and Poisson's ratio are computed as $E = 23.7$ MPa and $\nu = 0.1402$. The calibrated parameters are used for pure MPM simulation. Other material properties are shown in Table 2. The soil column is discretized into 50 uniform elements with a size of 0.02 m. The timestep size for the MPM solver is set as $\Delta t = 1 \times 10^{-4}$ s. Note that, to balance the initial stress in the RVE, we first apply a

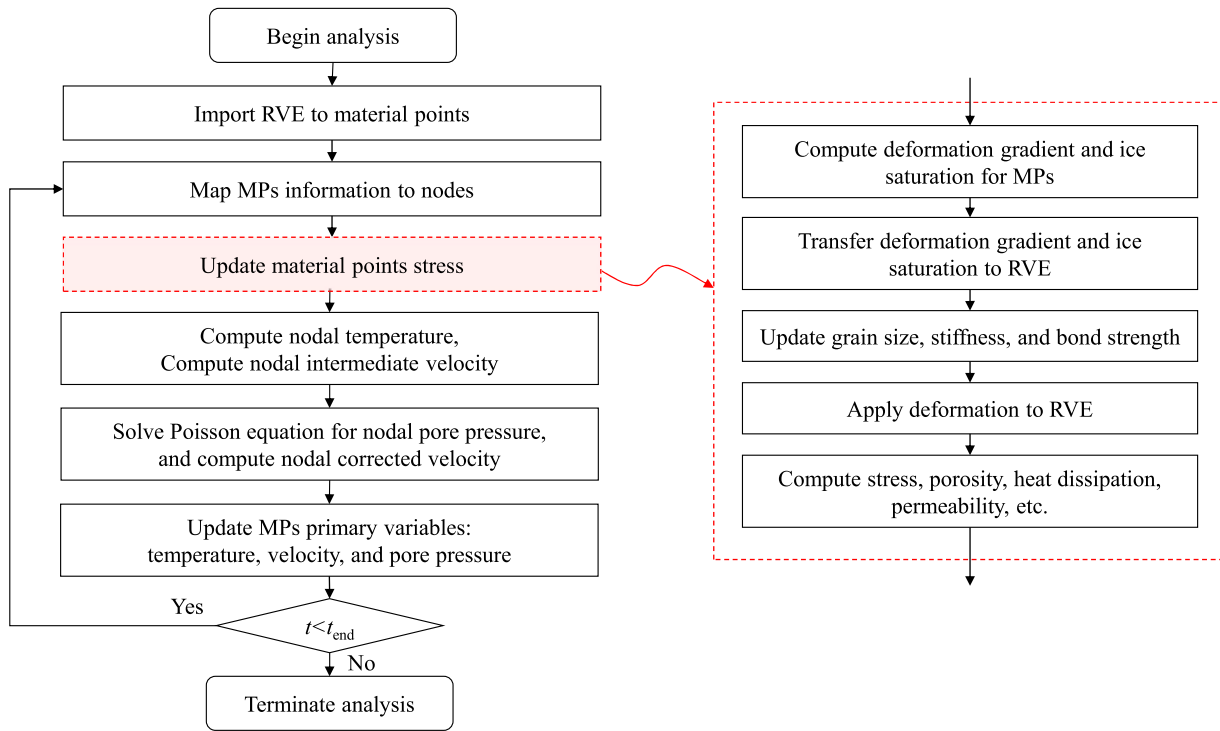


Fig. 5. Overall solution procedure for multiscale multiphysics approach by coupling MPM and DEM.

Table 1
Macroscopic parameters used for 1D non-isothermal consolidation problem.

DEM parameters	Value
Number of grains in an RVE, N_{grain}	400
Grain density, ρ_{grain} [kg/m ³]	2650
Grain size, r_{grain} [mm]	3–7
Young's modulus, E_c [MPa]	600
Poisson's ratio, ν_c	0.8
frictional coefficient, μ	0.5

Table 2
Microscopic parameters used for RVE preparation in 1D non-isothermal consolidation problem.

MPM parameters	Solid	Liquid	Ice
Young's modulus, E [MPa]	23.71		
Poisson's ratio, ν	0.1402		
Porosity, ϕ	0.1647		
Hydraulic conductivity, k_a [m/s]	1×10^{-3}		
Intrinsic density, ρ_s, ρ_l, ρ_c [kg/m ³]	2650	1000	917
Specific heat capacity, c_s, c_l, c_c [J/kg/°C]	4200	800	2060
Thermal conductivity, $\kappa_s, \kappa_l, \kappa_c$ [MW/m/°C]	2.4	0.6	2.2
Thermal expansivity, $\beta_s, \beta_l, \beta_c$ [1/°C]	1.5×10^{-5}	2.1×10^{-4}	1.53×10^{-4}

surface surcharge of 100 kPa on the soil column until its stress field reaches a steady state before prescribing further loads.

Fig. 7(a) shows the distributions of temperature at different time instances, and Fig. 7(b) shows the evolutions of temperature at different soil depths. Since the temperature solutions in Case 2 and Case 3 are almost identical due to small deformation, we only present the results of Case 2 for brevity. The surface displacement versus time and the pore pressure versus time/depth for all three cases are shown in Figs. 7(c) and 8, respectively. As can be seen, the MPM solutions and the MPM-DEM solutions are almost identical, and both are in good agreement with the analytical solutions. This indicates that the MPM solver and the newly developed MPM-DEM solver can offer accurate predictions.

Different displacement trends of the three cases, as shown in Fig. 7(c), are closely related to their pore pressure evolutions. Fig. 8(a)

and (d) plot the spatial distribution and the time evolution of pore pressure in Case 1 (the isothermal case) at representative soil depths and time instances, respectively. These results show typical pore pressure dissipation curves of Terzaghi's consolidation problem. The resulting consolidation curve, as shown in Fig. 7(c), is a natural outcome of the pore pressure dissipation under isothermal conditions. However, for Case 3, the non-isothermal case, a non-monotonical pore pressure dissipation pattern can be observed from Fig. 8(f), as the competing result of thermal expansion and pore pressure dissipation. The pure thermal expansion can generate a positive excess pore pressure, as indicated by Fig. 8(e). Besides, the pore pressure evolution curve for $z = 0.4$ m in Case 3 exhibits a clear turning point in the descending period, as can be observed in Fig. 8(f), while the curve in Case 2 displays a dual-peak feature, as can be observed in Fig. 8(e). This is a result of the superposition of the forward wave and the reflected wave from the bottom fixed boundary. If the simulated domain is infinite/absorbing boundary is adopted (Feng et al., 2021, 2022), the predicted pore pressure dissipation curves should be parallel, with identical peak values at different depths (McTigue, 1986; Yu et al., 2024a). Despite Case 2 showing an overall expansion trend as expected, its surface displacement witnesses a nontrivial peak, after which the soil turns to contraction. This is because the thermal expansion of pore water also contributes to the build-up of excess pore pressure and the expansion of the soil matrix at the early stage. However, with the dissipation of pore water, this part of contributions disappears gradually. Overall, it is demonstrated that the multiscale MPM-DEM framework can accurately simulate different THM-coupled problems.

6.2. 2D THM responses under cyclic thermal load

The response of soil subjected to cyclic thermal loading is of great importance for a wide range of engineering settings (Bai, 2006; Di Donna and Laloui, 2015; Ng et al., 2016; Bentil and Zhou, 2022). The second example further benchmarks the multiscale method by considering a 2D problem involving cyclic thermal loading. The simulated domain is rectangular with a dimension of 24 m × 9 m and an initial temperature of T_0 , as depicted in Fig. 9. The bottom boundary is fully

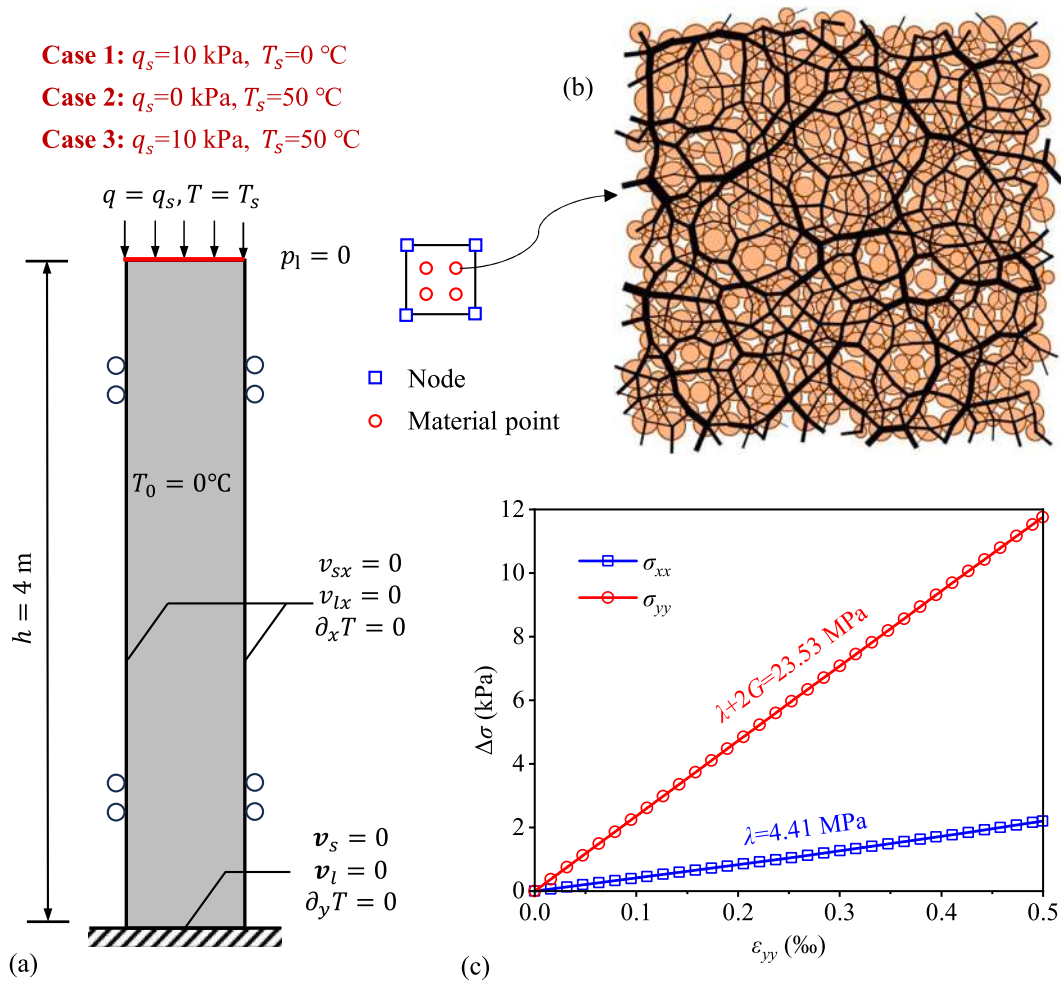


Fig. 6. (a) Model setup of the non-isothermal consolidation problem, (b) RVE packing, and (c) estimation of elastic parameters of the RVE.

fixed, while the vertical boundaries are fixed in the horizontal direction only. The simulated domain is subjected to a pile-like line heat source, as shown in Fig. 9. Since phase transition is not considered in this example, we set the initial temperature T_0 as 5°C and the inputting temperature (T_b) of the heat source periodically changing from 0°C to 10°C following a sinusoidal function $T_b = T_0 + T_1 = 5 + 5 \sin(2\pi t)$ to ensure the soil around the heat source experiencing cyclic cooling and heating. Five cycles are conducted in the simulation. Due to geometric symmetry, we simulate only half of the domain. A uniform background mesh with a cell size of 0.2 m and four material points in each cell is used. For MPM-DEM simulation, a surface surcharge of 100 kPa is imposed on the top surface to balance the initial stress of the embedded RVE in each material point. The initial RVE packing and the macroscopic parameters used in this example are largely the same as those in Section 6.1, except the following four parameters: $k_a = 1 \times 10^{-10} \text{ m/s}$, $\kappa_s = 2.4 \text{ W/m}^\circ\text{C}$, $\kappa_l = 0.6 \text{ W/m}^\circ\text{C}$, and $\kappa_c = 2.2 \text{ W/m}^\circ\text{C}$ (will be used in Section 7). To accelerate the simulation, the four parameters are scaled by 365×86400 times. As it is difficult to derive the analytical solution for this complex boundary value problem, we consider verifying the simulation result of the MPM-DEM approach by comparing it with the MPM solution. The accuracy of the MPM solver for modeling THM-coupled problems has been extensively examined in our previous work (Yu et al., 2024a).

The contours of pore pressure simulated by MPM-DEM and pure MPM at four representative time instances in the first cycle are shown in Fig. 10. The evolution of pore pressure and vertical displacement at points M0 ($0 \text{ m}, 6 \text{ m}$), B6 ($6 \text{ m}, 0 \text{ m}$), and M6 ($6 \text{ m}, 6 \text{ m}$) are plotted in Fig. 11(a) and (b), respectively. From 0 to 0.25 s , points

M0 and M6 are displaced downward due to thermal contraction as the temperature decreases. Correspondingly, negative pore pressures are generated near the heat boundary, as indicated by the contour map in Fig. 10(a) and the extracted data at point M0. However, the response of pore pressure at the faraway point B6 exhibits a delayed and reduced evolution. After the cooling stage, the inputting temperature returns to its initial level. The pore pressure near the boundary tends to become positive, while the negative zone tends to shift away to the far end (see Fig. 10(b)). While the inputting temperature continues increasing to the peak value, the expansion-dominated deformation pattern is transferred to a contraction-dominated one, with the pore pressure showing a nearly opposite distribution (see Fig. 10(c)) compared to the cooling stage (see Fig. 10(a)). It is also found from Fig. 11 that the level of the peak points in the first and second cycles show slight differences, while these differences become less significant in the third to fifth cycles, indicating the cyclic response reaching a stable state.

Overall, the simulation results in the first cooling–heating cycle and all five cycles are reasonable. The good agreement between results obtained from the MPM-DEM solver and pure MPM solver also highlights that the proposed multiscale framework is effective when dealing with complex boundary problems and can be readily used to model more complex phase transition problems.

7. Multiscale modeling the freeze-thaw behavior of ice-bonded granular media

In this section, we revisit the example in Section 6.2 by considering phase transition to showcase the method’s predictive capability in

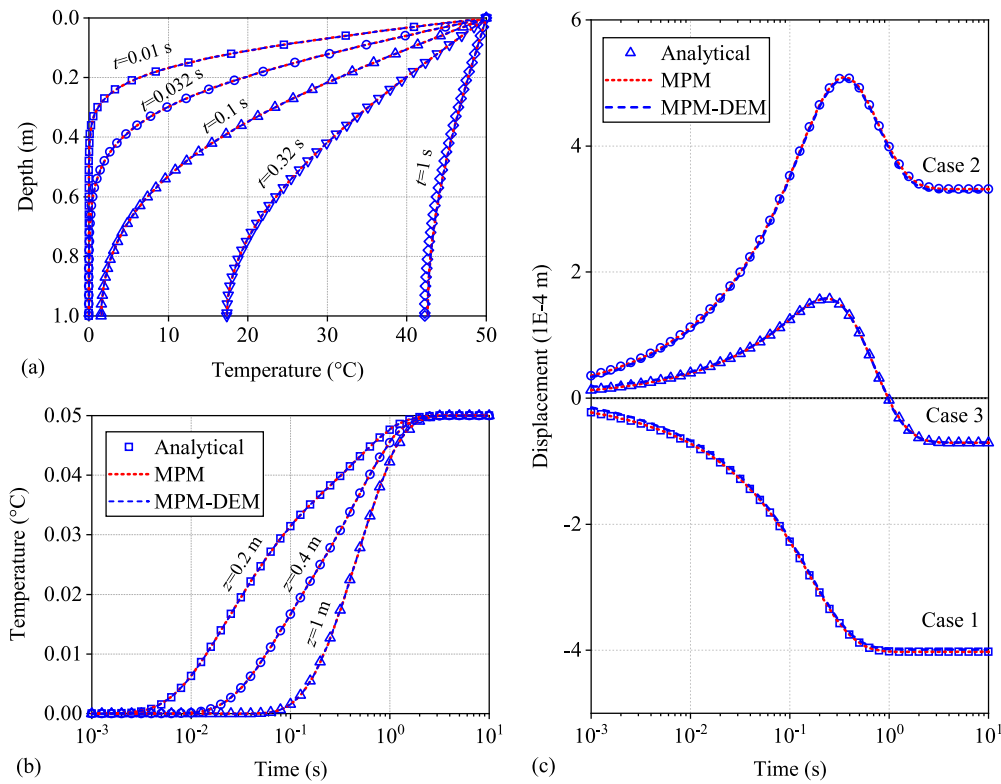


Fig. 7. (a) Temperature distribution at $t = 0.01, 0.032, 0.1, 0.32,$ and 1 s; (b) temperature evolution at depths of $0.2, 0.4,$ and 1 m in Case 2; (c) surface displacement in three cases.

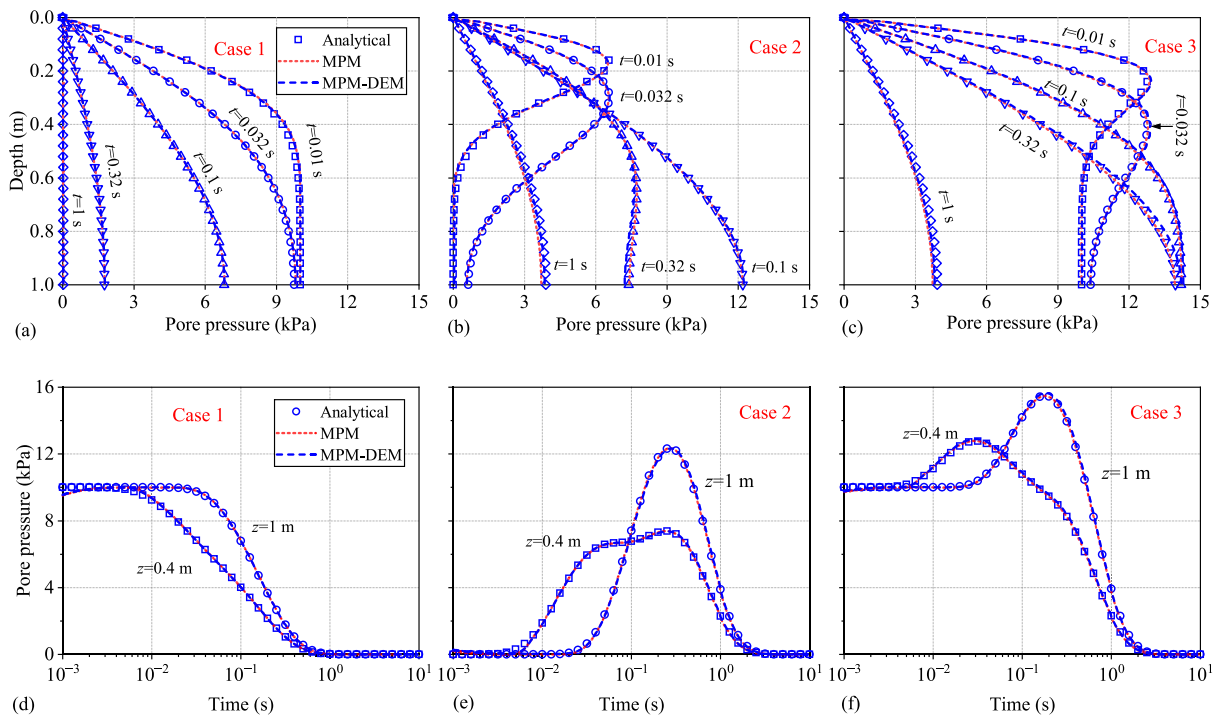


Fig. 8. Pore pressure distribution in (a) Case 1, (b) Case 2, and (c) Case 3 at the elapsed time of $0.01, 0.032, 0.1, 0.32,$ and 1 s, and pore pressure evolution versus time in (d) Case 1, (e) Case 2, and (f) Case 3 at depths of 0.4 m and 1 m.

simulating ice-bonded granular media under freeze-thaw cycles. The geometry remains unchanged, as depicted in Fig. 9, while the initial temperature T_0 is set to 0 °C and the corresponding temperature input, $T_0 + T_1$, varies from -5 °C to 5 °C. The basic DEM parameters are

identical to those employed for the RVE in Section 6.1. Supplementary parameters specific to the ice bonds are provided in Table 3. In this example, we consider the soil nearly cohesionless in its unfrozen state, resembling sandy soil. Therefore, a very small unfrozen cohesion

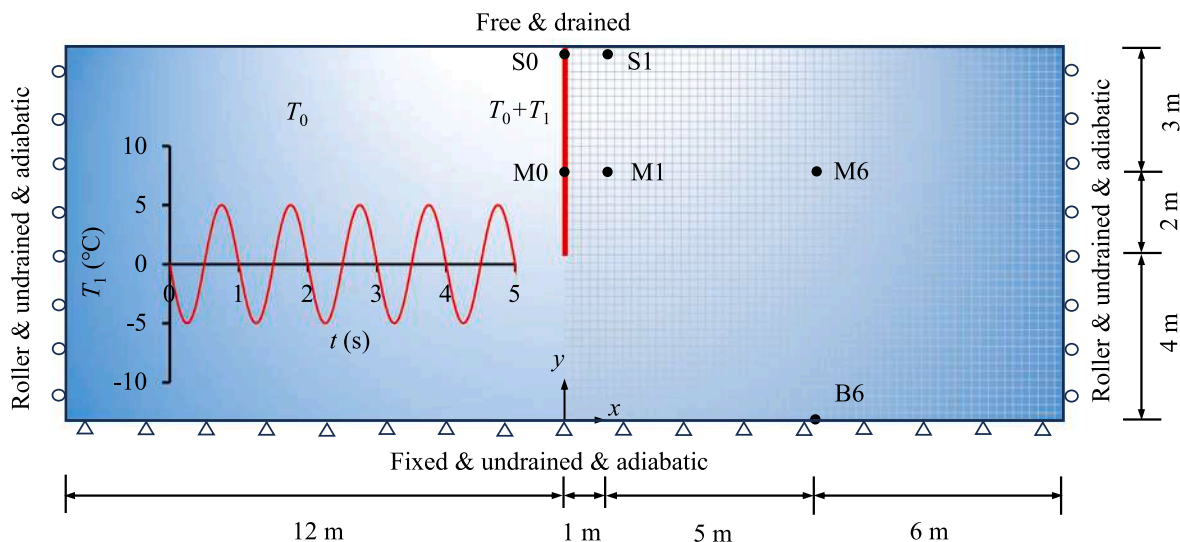


Fig. 9. Model setup of the cyclic thermal loading example.

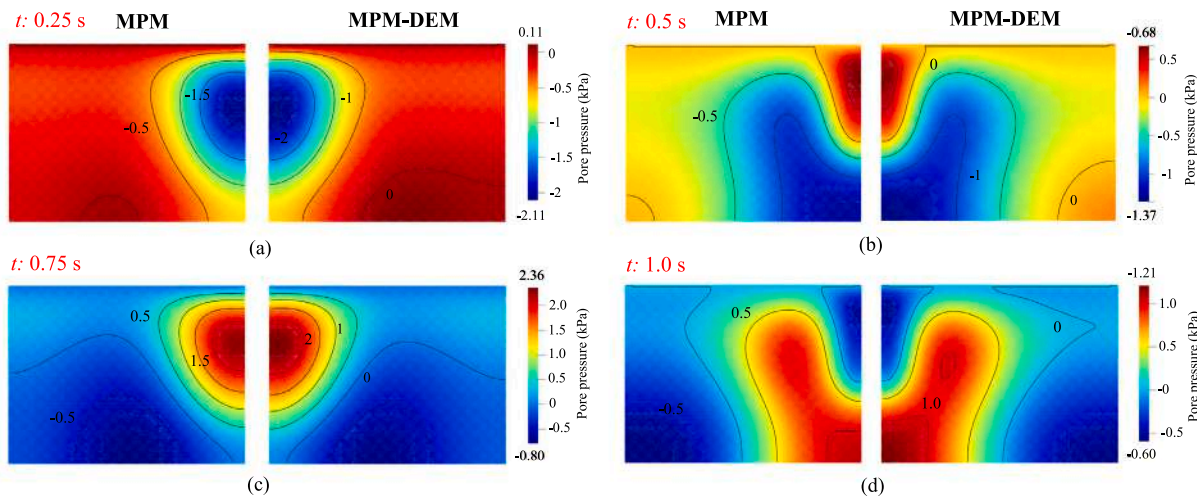


Fig. 10. Comparison of excess pore pressure contour solved by MPM-DEM and MPM at representative time instances in the first cycle.

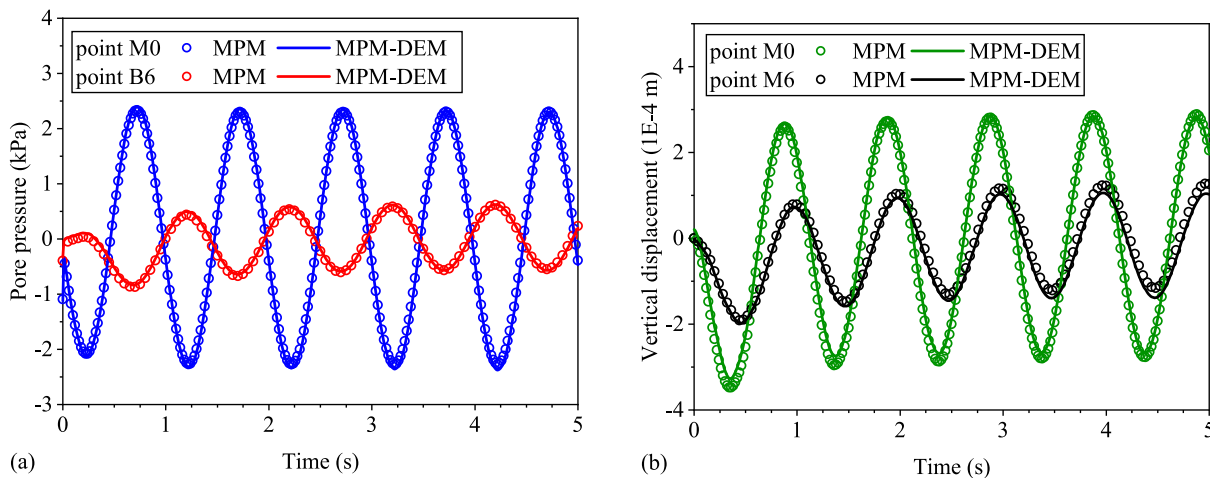


Fig. 11. Comparison of (a) pore pressure and (b) vertical displacement solved by MPM-DEM and MPM at selected points.

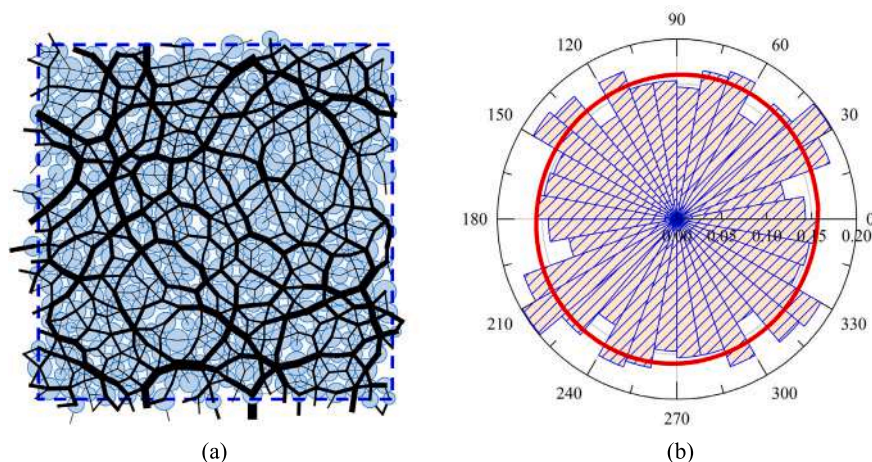


Fig. 12. (a) The force chain of the initial RVE packing and (b) the rose diagram of the contact normal orientation. The red line shows the best Fourier approximation.

Table 3
Parameters for the saturation-dependent bond contact model.

DEM parameters	Value	
Young's modulus	E_{c0}	0.6 GPa
	ΔE_c^{max}	3.0 GPa
	C_{i0}	0.2 MPa
Cohesion strength	Case 1: weak ice bond	25 MPa
	ΔC_i^{max} Case 2: medium ice bond	50 MPa
	Case 3: strong ice bond	100 MPa
Number of grains in an RVE, N_{grain}	420	
Initial porosity, ϕ_0	0.1633	

strength, C_{i0} , is utilized. The young's modulus of soil grains in an unfrozen state, E_{c0} , is assigned the same value as in Section 6.1, while its maximum additional value under a frozen state, ΔE_c^{max} , is set as 5 times of E_{c0} . To examine the role of ice bond on the global THM responses, we simulate three cases with varying maximum bond strength, i.e., $\Delta C_i^{max} = 25, 50,$ and 100 MPa, denoted as the weak bond case, the medium bond case, the strong bond case, respectively. The parameters utilized in this study fall within the typical range of DEM parameters employed in the literature for simulating ice-rich soil (Zhu et al., 2021; Chang et al., 2023; Sun et al., 2023). The frictional contact model is first used to prepare a dense RVE packing under a confined stress of 100 kPa, and then the cohesive bond contact is activated for the freeze-thaw simulation. The force chain of initial RVE packing and the contact normal distribution are shown in Fig. 12. The Fourier approximation (red line) shows the initial RVE is isotropic.

7.1. Macroscopic THM responses

7.1.1. Thermal responses

In the THM simulation of frozen soils, an accurate simulation of the temperature field is crucial for ensuring correct modeling of other fields. The typical temperature fields for the strong ice bond case during the first freeze-thaw cycle in strong ice bond case in Fig. 13(a). It is found the temperatures at different stages change correspondingly to varying boundary conditions, exhibiting generally reasonable thermal fields. Fig. 13(b) further plots the temperature at M0 (0 m, 6 m), M1 (1 m, 6 m), M2 (2 m, 6 m), and M3 (3 m, 6 m) over time. Point M0 is rightly positioned on the temperature boundary, whereas points M1 to M3 are located progressively away from the boundary. The temperature evolution at point M0 displays a perfectly harmonics shape with peak values of about 5 °C and -5 °C, as the most immediate response to the boundary temperature input. However, at points M1 and M2, the temperature evolution deviates from the perfect sinusoidal curve due to the latent heat effect, while at point M3, the temperature change

becomes less pronounced, indicating a reduced impact from the temperature boundary. The thermal response in the rest four cycles exhibits a similar trend for other cases. Minor discrepancies may be found because deformations, especially large deformations, can potentially impose certain impacts on the thermal field. However, a detailed discussion on this aspect will not be conducted as it is beyond the scope of this study.

7.1.2. Mechanical responses: frost heave and thaw settlement

This subsection focuses on the deformation patterns, particularly on the frost heave and thaw settlement, which represent two important mechanical behaviors of soils subjected to freezing and thawing (Nishimura et al., 2009; Zhang et al., 2015; Na and Sun, 2017). The vertical displacements at point S0 (0 m, 9 m), the midpoint of the ground surface in three cases, are shown in Fig. 14. The selected point represents the most severely deformed area in the entire simulation domain. In each freeze-thaw cycle, the vertical displacement at point S0 increases first during the freezing stage and then recovers partly in the thawing stage. The freezing-induced heave and thawing-induced settlement, in mesoscale, correspond to, respectively, the contraction and expansion of RVEs attached to the material points. The phenomenon that the deformation will not return to its initial value is attributed to the microscopic changes during the freeze-thaw cycles, such as particle rearrangement and bond breakage (Viklander, 1998). Such particle-level influences are not easy to be captured by continuum-based modeling.

Comparing all three parallel cases, the magnitude of frost heave is greatly influenced by the ice bond strength of RVEs. Among them, the weak bond case displays the most substantial frost heave during the first cycle and the most rapid accumulation of heave amount in repeated cycles. In contrast, the strong bond case shows no noticeable increase in the overall heave amount with repeated cycles. This implies that the plastic deformation in the weak bond case continuously accumulates with increasing cycles, whereas, in the strong bond case, it mainly accumulates in the first cycle. To better illustrate the discrepancies, we present the contours of vertical displacement at $t = 0.5, 1.5, 2.5,$ and 3.5 s in Fig. 15. The associated time instances approximately correspond to the time when the frost heave reaches the utmost in each freeze-thaw cycle. It can be seen that for the strong bond case, the displacement fields in all cycles show almost no changes, whereas the changes with cycles in the resting two cases are relatively prominent. This is because a weak ice bond in RVEs may fail to resist a large heave force, resulting in more bond breakage and more RVE expansion. It is worth mentioning that the severe deformation in the weak bond case led to the breakdown of the simulation in the fifth cycle, mainly because of the failure of near-surface RVEs under superextreme deformations.

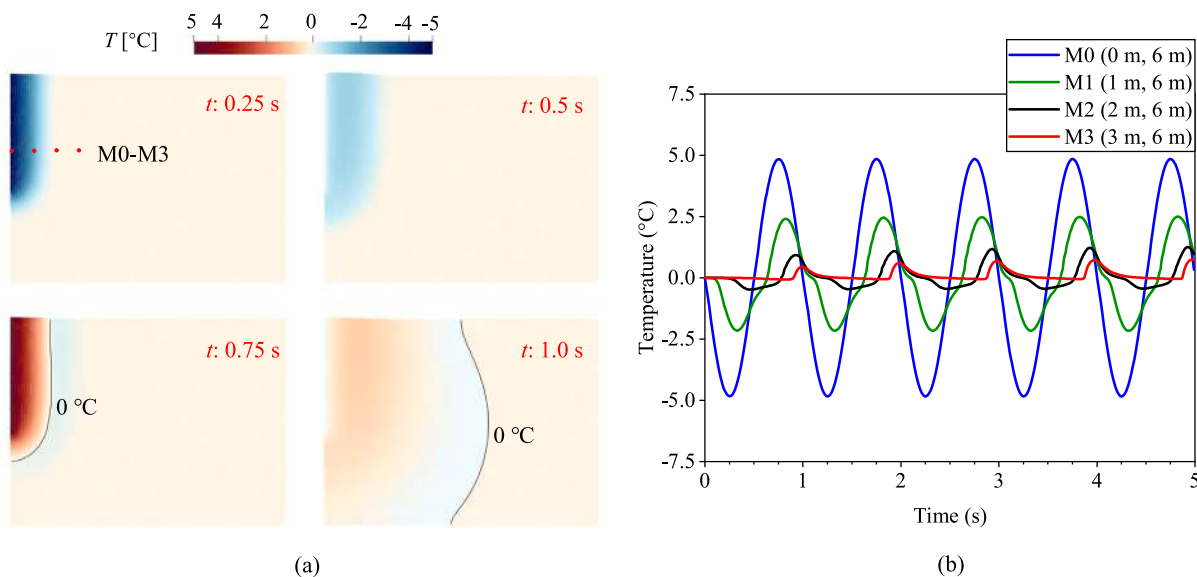


Fig. 13. (a) Contours of temperature in the first cycle and (b) evolutions of temperature at points M0–M3 in the strong bond case.

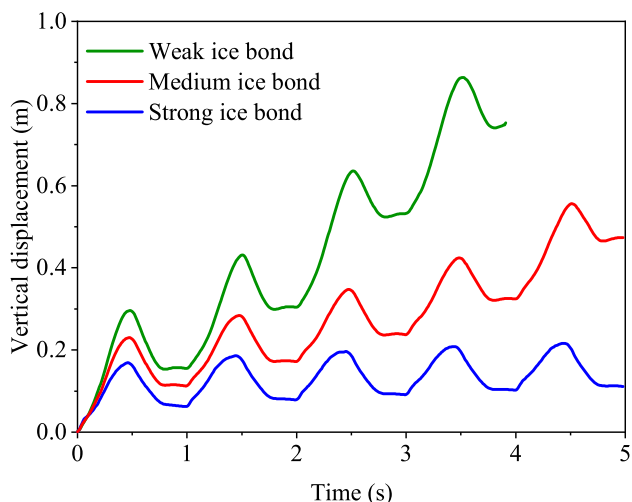


Fig. 14. Vertical displacement at point S0 (0 m, 9 m) on the ground surface.

Additionally, to further visualize the deformation of material points in the inner regions, we plot the trajectory of point M1 in the medium bond case and the strong bond case in Fig. 16. The mobilization of material points follows a hysteresis loop but not a close one. Obviously, the point in the medium bond case experiences more movements in both lateral and vertical directions. Besides, the movement of the point in the strong bond case shows a convergent trend, while the one in the medium bond case does not. In general, these findings are consistent with the previous analyses. Overall, typical deformation behaviors of soils under freeze-thaw cycles can be well-captured by the proposed multiscale method. Importantly, these mechanical behaviors can be connected with the particle scale responses, which will be further discussed in the following sections.

7.1.3. Pore pressure evolutions

The frost heave and thaw settlement during freeze-thaw processes are closely related to the pore water pressure. Fig. 17 shows the contours of pore pressure at $t = 0.25, 0.5, 0.75,$ and 1.0 s in the first freeze-thaw cycle. The most pronounced changes in pore pressure distribution are observed near the freeze-thaw boundary. However, the

trends of these changes differ significantly among the three cases. The most obvious discrepancy is the sign of pore pressure. For example, at $t = 0.25$ s, the pore pressure in the weak bond case is positive, while in the strong bond case, it is largely negative. At $t = 0.75$ s, the pore pressure in the weak bond case changes to negative, while in the strong bond case, it changes to positive. The medium bond case presents a transitional pattern from the strong to the weak bond cases. Figs. 18 and 19 further show the evolution of pore pressure over time at points M0 and M1. The pore pressure response is largely dependent on temperature changes and the bond properties of RVEs. The evolution of pore pressure in one freeze-thaw cycle, as shown in Figs. 18(a) and 19(a), can be generally divided into five stages.

- **Stage I:** The pore pressure increases slightly to a maximum value of about 100–150 kPa at the initial freezing stage. The increasing stage is widely observed in laboratory tests and is named as the free water freezing stage (Eigenbrod et al., 1996; Zhang et al., 2015). In this stage, the ice content increases quickly, wherein the positive pore pressure can be related to the volume expansion during increased ice nucleation.
- **Stage II:** The initially increasing pore pressure decreases with continuous freezing. The pore pressure in the strong bond case drops the most significantly among the three cases, and eventually, negative pore pressure develops, with a minimum value of about -350 kPa. The negative pore pressure is also recorded in experiments by Eigenbrod et al. (1996) and Zhang et al. (2015), usually explained as the cryogenic effect (Zhou and Meschke, 2013). In this simulation, the increasing ice content during the freezing stage enhances the bonds between soil grains, resisting the continuous heave of the soil, thereby leading to a pressure drop and even generating a negative pore pressure when the bonding effect is very strong. In the authors' opinion, the bonding effect describes similar phenomenon as the cryogenic effect.
- **Stage III:** After a dramatic decrease, the pore pressure reaches a relatively stable state with some dissipation over time as the ice content reaches a stable (maximum) value. Specifically, the pore pressure gradually increases in the strong bond case and decreases in the weak and medium bond case. The duration of this stage depends on how long the freezing stage can be maintained (e.g., M0 is longer than M1).
- **Stage IV:** The pore pressure experiences a second sharp change as a result of a rapid increase in temperature and an accelerated melting of ice. In this stage, the strong bond case is featured by a

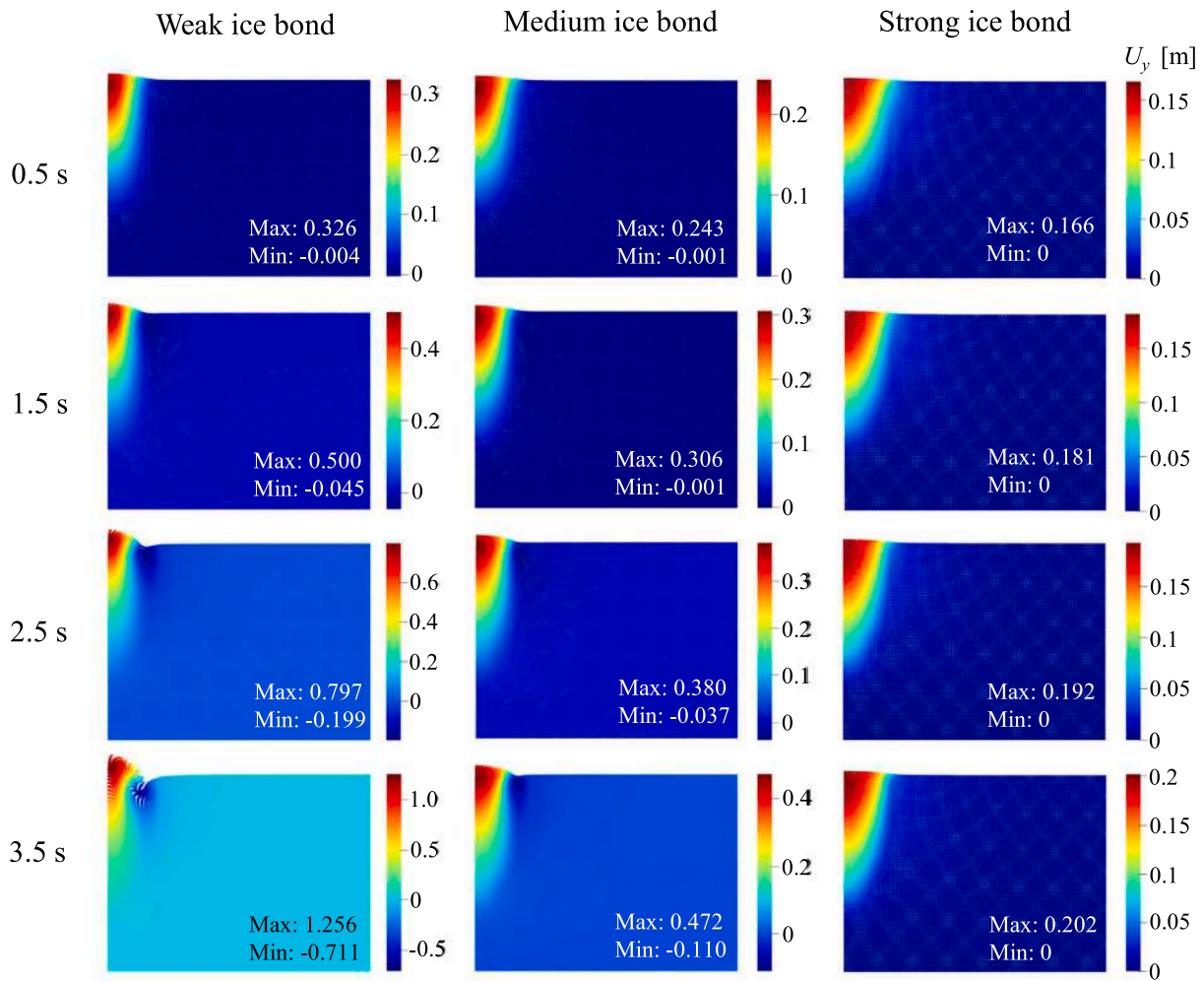


Fig. 15. Contours of vertical displacement after the freezing stage in each cycle.

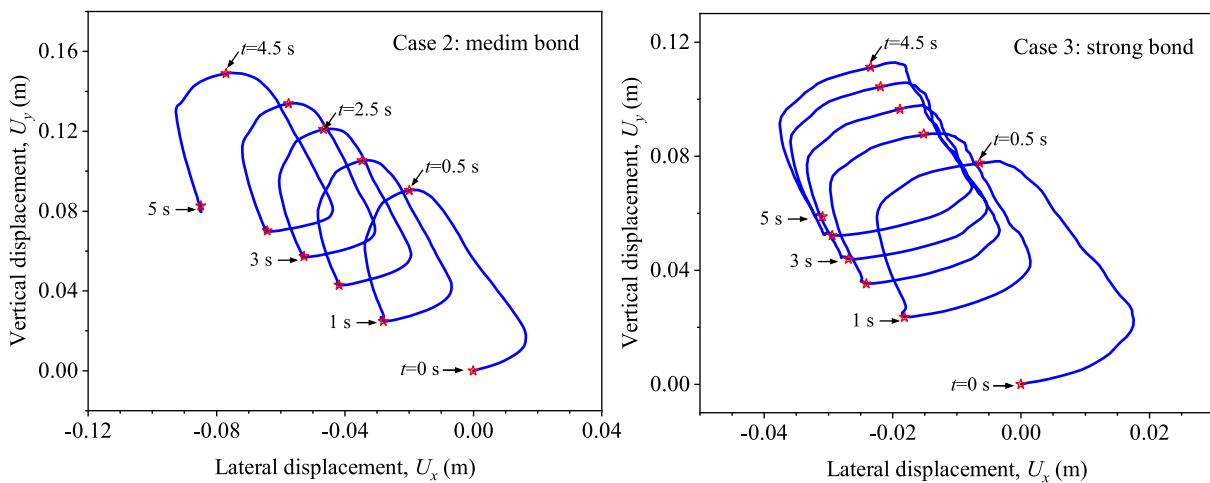


Fig. 16. Trajectory of point M1 in the medium (left) and the strong (right) bond case.

rapid pore pressure increase due to the loss of the ice bond and effective stress, which is also observed in the experimental study performed by Zhang et al. (2014). In contrast, the weak bond case is featured by a rapid pressure drop, and the resulting negative

pore pressure tends to become larger with more freeze-thaw cycles, as indicated by Figs 18(b) and 19(b).

- **Stage V:** With the temperature continuously increasing, the pore pressure of all three cases approaches zero. The pore pressure in

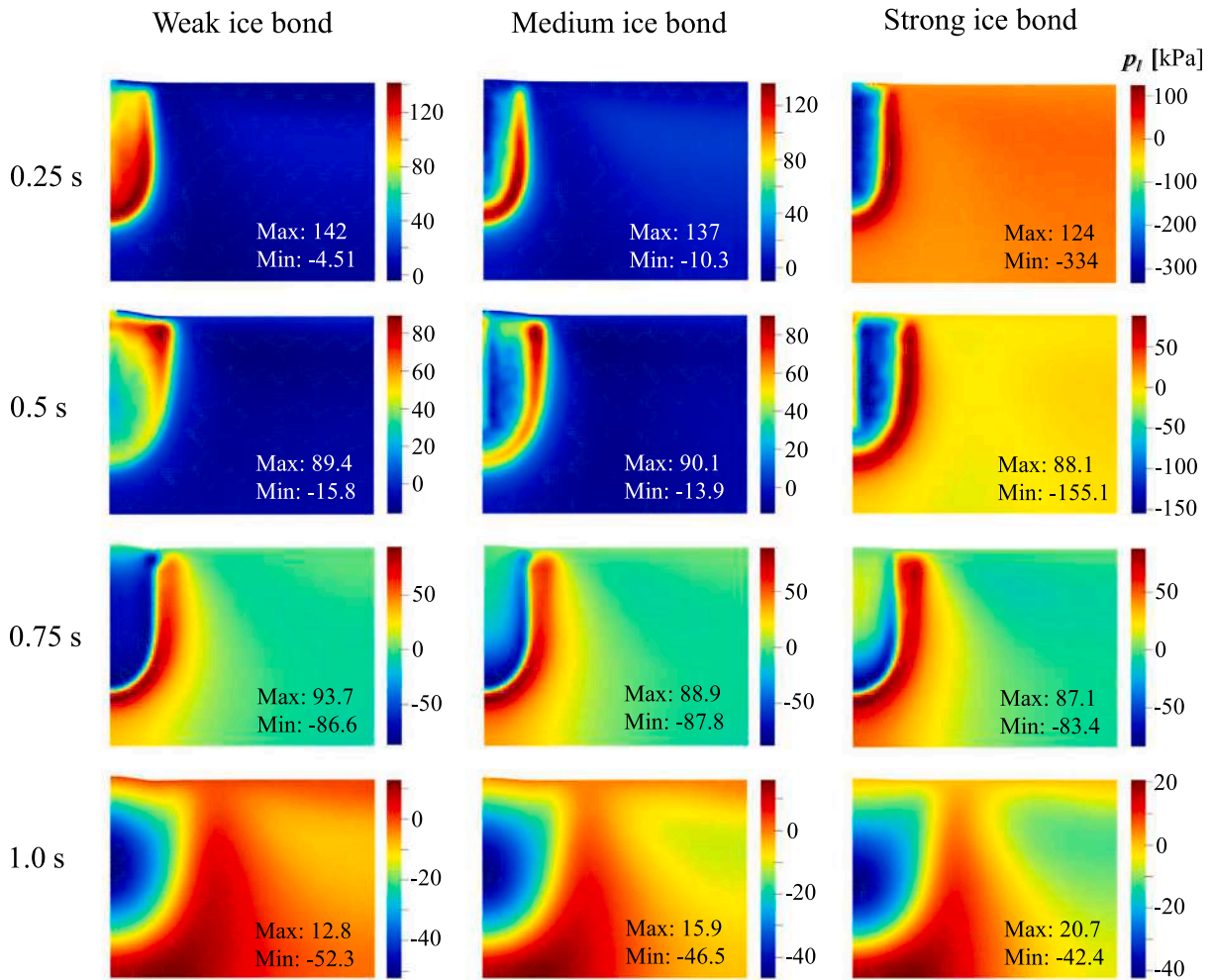


Fig. 17. Contours of pore pressure at representative time instances in the first freeze-thaw cycle.

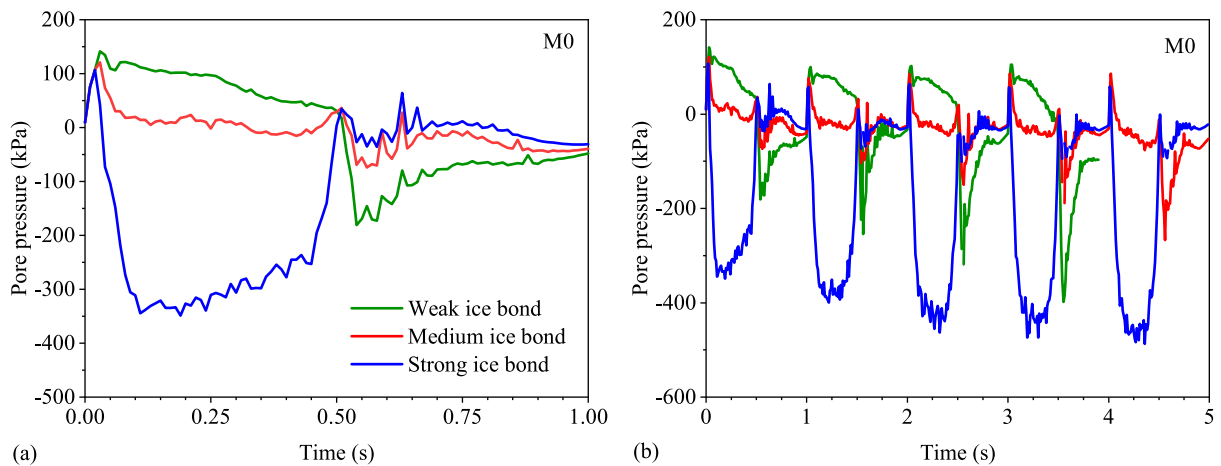


Fig. 18. Pore pressure at point M0 (0 m, 6 m) in (a) the first cycle and (b) all five cycles.

this stage for all three cases shows almost unified distributions, as indicated by the contours for $t = 1.0$ s in Fig. 17.

The five stages represent typical pore pressure changes occurring within one freeze-thaw cycle. The diverse pore pressure responses

observed in cases with different ice bonds reflect the varying freeze-thaw characteristics of soils when the role of ice role differs. The strong bond case shows the best match with most of the experimental studies on soils upon freezing and thawing. This highlights the effectiveness of the presented multiscale method and also the importance of correctly

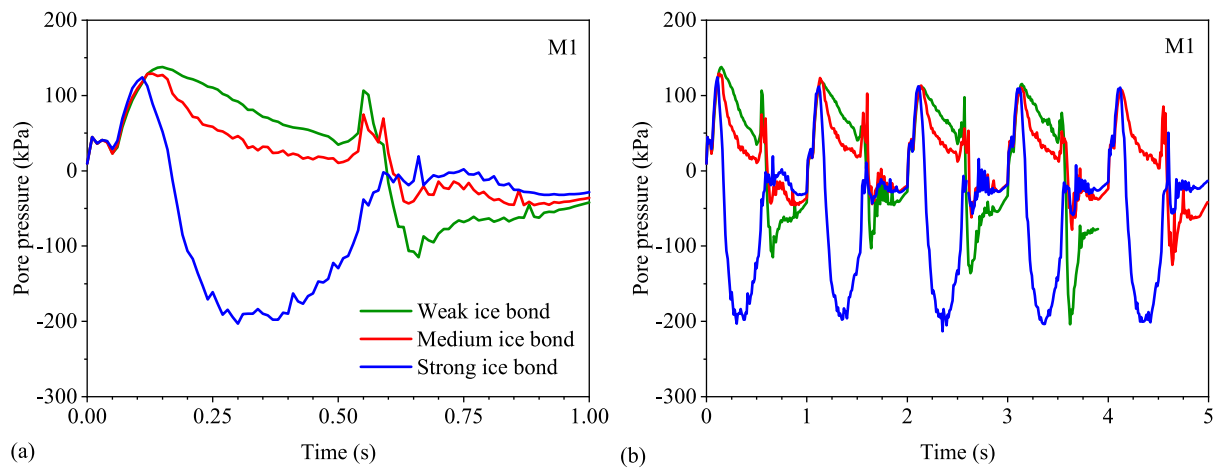


Fig. 19. Evolution of pore pressure at point M1 (1 m, 6 m) (a) in the first freeze-thaw cycle and (b) in five freeze-thaw cycles.

considering the ice bonding effect in DEM model. However, it does not mean the responses of the other two demonstrative cases are meaningless because the strength of ice bonds in soils is dependent on many factors, including soil type, water content, soil porosity, loading path, and stress state, etc. (Wang et al., 2008; Liu et al., 2019; Zhang et al., 2016, 2020).

7.2. Strain–stress characteristics and RVE responses

7.2.1. Strain–stress characteristics

A major contribution of this work is employing the physics-based DEM approach instead of a phenomenological constitutive model to describe the material response. In this section, we further investigate the evolutions of strain and stress during the freeze-thaw loading. Fig. 20 shows the volumetric strain ε_v , mean effective stress σ_v , deviatoric strain ε_d , and deviatoric stress σ_d , in the first cycle and all five cycles. Considering that the results of the weak and the medium bond cases are quite similar, we present only the medium and the strong bond cases.

The volumetric strain in one freeze-thaw cycle includes four stages, as shown in Fig. 20(a). The following takes point M0 in the strong bond case in the first cycle as an example (the red dotted line). (1) Before about 0.05 s, the volumetric strain increases rapidly due to ice formation, corresponding to pore pressure Stage I. (2) From about 0.05 s to 0.45 s, the volumetric strain maintains constant at about 2.5%, corresponding to pore pressure Stage II and III. (3) From about 0.45 s to 0.5 s, the volumetric strain drops rapidly as the temperature rises; this stage is an inverse process of the first stage, corresponding to pore pressure Stage IV. (4) After 0.5 s, the volumetric strain changes at a very low rate, corresponding to pore pressure Stage V. The four stages represent the typical volumetric changes in one freeze-thaw cycle. The curve of M1 is a bit delayed compared to that of M0 because of the temperature difference, as indicated by Fig. 13. Almost identical volumetric behaviors are observed in the one-dimensional freeze-thaw tests performed by Nishimura et al. (2021) (cf. Figure 5 in the reference paper). Besides, it is found that the curves for the medium bond case and strong bond case are almost identical in the first cycle. However, their gap tends to become increasingly large in the following cycles. In addition, the volumetric strain after each freeze-thaw cycle tends to converge at a constant negative value. For instance, at point M0, the magnitude of peak volumetric strain in the thawing stage is stabilized at about -2% . The volumetric shrinkage phenomenon is widely documented in experimental studies (Konrad, 1989; Viklander, 1998; Qi et al., 2006, 2008; Nishimura et al., 2021). This can be explained as a consequence of particle rearrangement after freeze-thaw loading by Viklander (1998), which can be naturally simulated by the presented multiscale approach.

The mean effective stress in Fig. 20(b) shows the same change trend as the pore pressure. The initial mean effective stress is -100 kPa (negative indicates compression), equaling the confined stress of RVE. In the first freeze-thaw cycle, the mean effective stress first decreases (in magnitude), and thus, the RVE is in a tensile state. This leads to a rapid volumetric dilation of RVE until the ice bonds between grains are built up. Correspondingly, the RVE becomes increasingly looser. When the volumetric strain reaches the stable state, the mean effective stress begins to increase, with the RVE changing from a tensile state to a compressive state. The compressive force on the RVE is induced by the ice bond-induced tensile force. Since a strong bond can undertake a much larger force without failure, the RVE in the strong bond case can bear relatively large mean effective stress and negative pore pressure. Followed is a stabilized stage and another stage with sharply changing effective stress as a result of the rapid thawing. Finally, the mean effective stress returns to the same level as the initial stress, around 100 kPa, with the soil subjected to continuous thawing. Apparently, the response of mean effective stress is closely related to the evolution of pore pressure.

Unlike the volumetric strain, the deviatoric strain in one freeze-thaw cycle presents only two evident stages — an increasing and a decreasing stage, as depicted in Fig. 20(c). The two stages correspond to the freezing and thawing processes, respectively. The shear strain developed during the freezing stage is attributed to the differential frost heave and geometrical effect (Nishimura et al., 2021). In the first cycle, the medium and the strong bond cases exhibit almost identical deviatoric strains. However, with repeated cycles, the fluctuation of deviatoric strain in the strong bond case reaches a balance, whereas, in the medium bond case, the deviatoric strain continuously increases. The phenomenon is observed in the results of both points M0 and M1. The shear stress in the medium bond case is also lower than that of the strong bond case, as shown in Fig. 20(d). These phenomena can all reflect that the bond strength directly influences the shear strength of the RVE and the deformation pattern of the macroscopic samples. This case demonstrates that the multiscale method can capture typical and reasonable mechanical responses. Nonetheless, it could be necessary to determine ice bond strength between grains if one aims to perform a realistic case study.

7.2.2. RVE responses

To offer a deep understanding on how the RVEs evolve during freeze-thaw cycles and how the deformation patterns of RVEs are related to the mesoscopic responses, we further investigate the RVE responses in some representative regions. Four typical RVEs are selected in regions S0 (0 m, 9 m), S1 (1 m, 9 m), M0 (0 m, 6 m), and M1 (1, 6 m). S0 and S1 are positioned near the ground surface, representing the

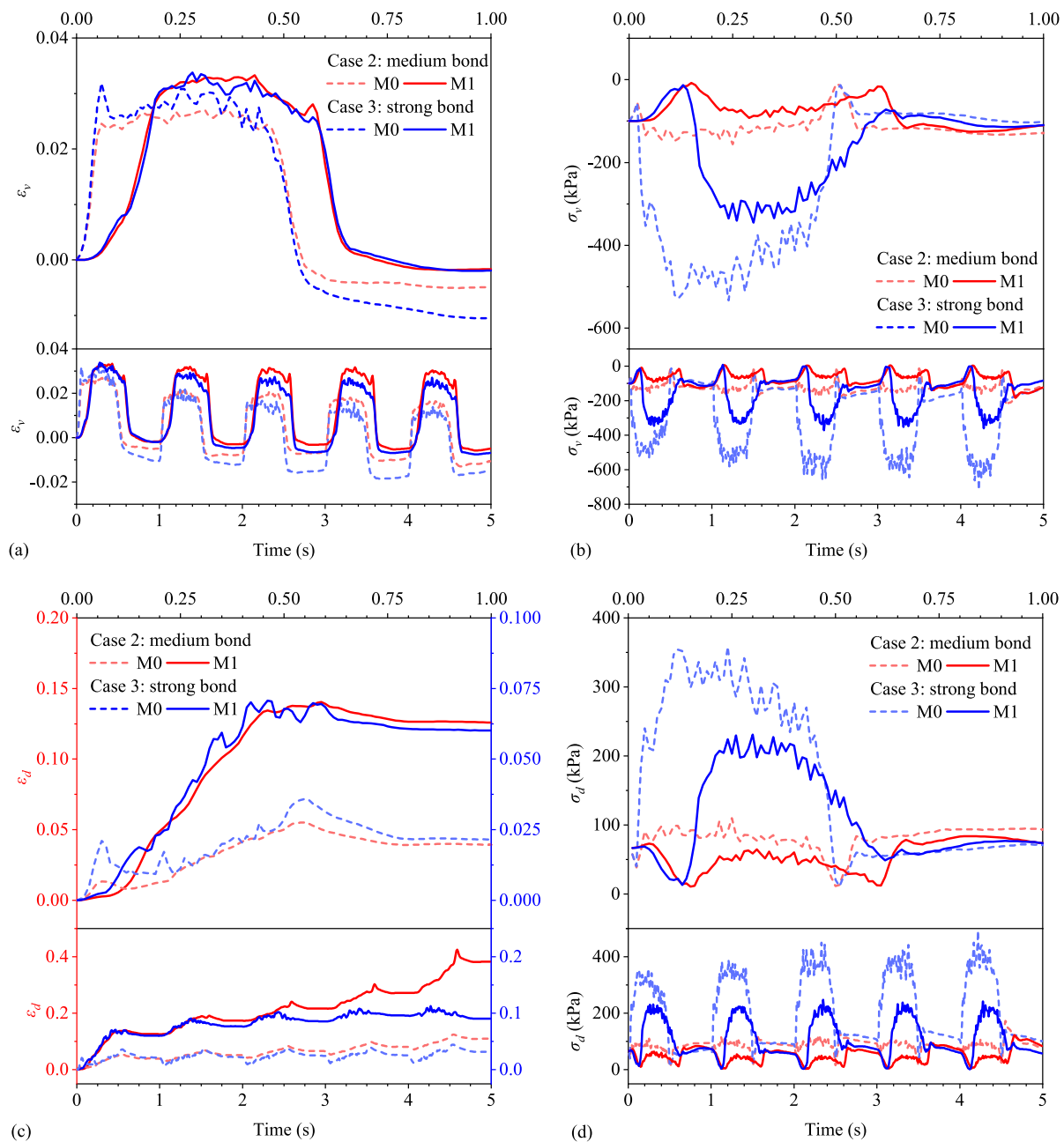


Fig. 20. Evolution of (a) volumetric strain ϵ_v , (b) mean stress σ_v , (c) deviatoric strain ϵ_d , and (d) deviatoric stress σ_d at points M0 (0 m, 6 m) and M1 (1 m, 6 m) in the medium bond case and the strong bond case. For each subfigure, the bottom part shows the results of all five cycles, while the upper part shows the zoomed plot of results in the first cycle.

severely deformed areas due to frost heave. The displacement of point S0 has been presented in Fig. 14 and analyzed in Section 7.1.2. The THM responses at points M0 and M1 have been thoroughly analyzed in previous sections. Generally, the weak bond case shows the most significant RVE deformation among the three cases, while the strong bond case shows the least significant deformation. However, their RVE deformation patterns are quite similar. The following will focus on the medium bond case as an example.

The forces chain network and the contact normal distribution for the four selected RVEs after 1, 3, and 5 cycles are shown in Figs. 21 and 22. The RVEs at associated points show increasingly severe deformations with increasing freeze-thaw cycles, especially for points S0 and S1, as evident by Fig. 22(a) and (b). Such large deformation behaviors may not be well-captured by conventional phenomenological-based

and small strain-based constitutive models, whereas the current multiscale method does not suffer from this limitation. The selected RVE points show rather different deformation patterns. Wu et al. (2020) proposed that the mesoscale deformation features of each RVE can be decomposed into three components: (1) compaction or extension, (2) simple shear deformation, and (3) rigid-body rotation. As seen from Fig. 21, the RVE at point M0 is in a compaction/extension-dominated deformation pattern, while at point M1 is in a combined compaction/extension and simple shear pattern. These RVE responses are consistent with the characteristics that the deviatoric strain of M1 is greater than that of M0, as shown in Fig. 20(a) and (c). The extension of soils near the freeze-thaw boundary, represented by points M0 and M1, is responsible for the global frost heave in the vertical direction. Besides, it is evident that M0 experiences more compaction in the X-direction (more extension in the Y-direction) compared to M1, resulting

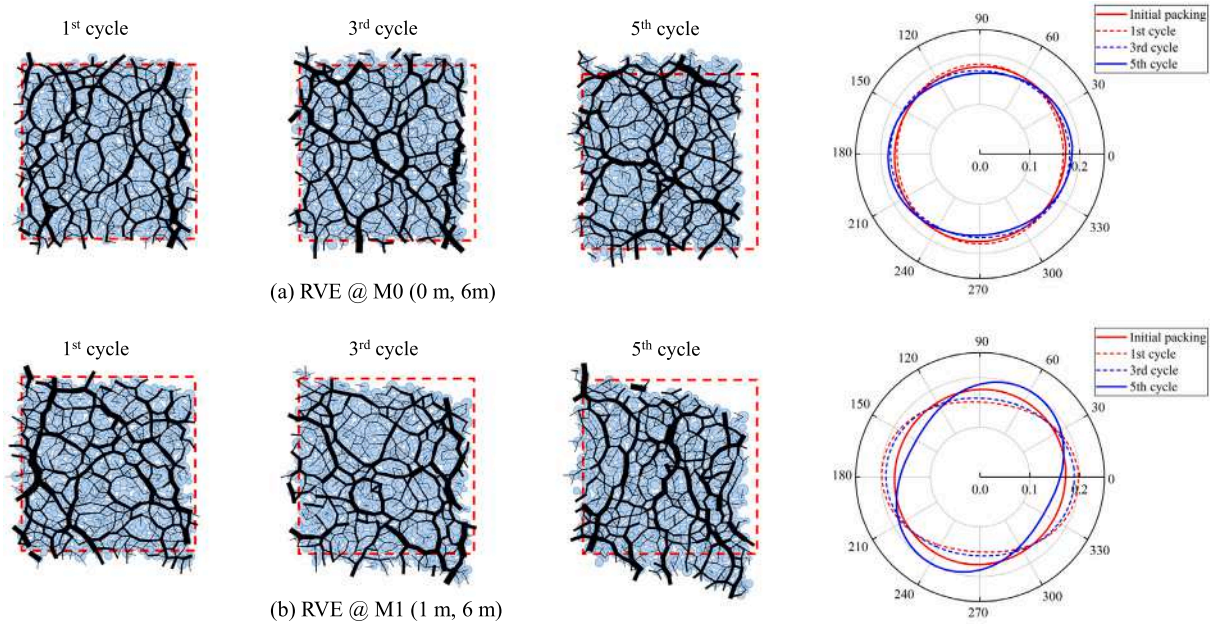


Fig. 21. Deformed RVEs with force chains normalized by average normal contact force and the corresponding rose diagram of contact normal orientations at point (a) M0 (0 m, 6 m) and (b) M1 (1 m, 6 m) in the medium bond case after the first, third, and fifth cycle.

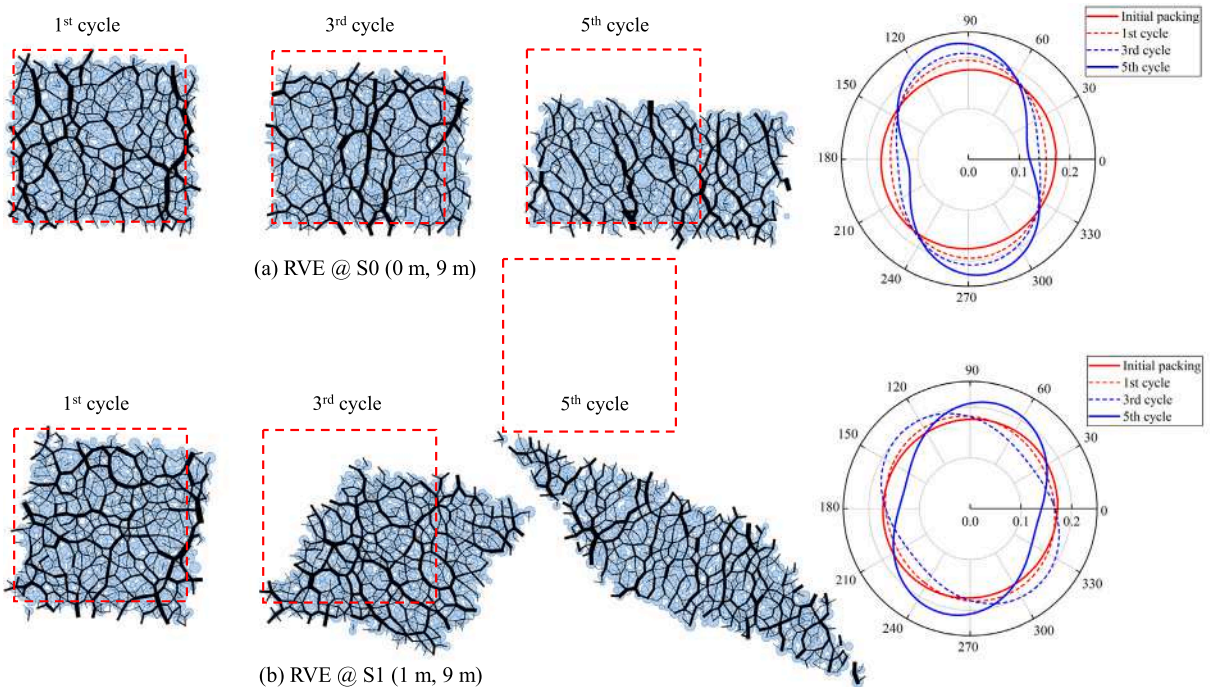


Fig. 22. Deformed RVEs with force chains normalized by average normal contact force and the corresponding rose diagram of contact normal orientations at point (a) S0 (0 m, 9 m) and (b) S1 (1 m, 9 m) in the medium bond case after the first, third, and fifth cycle.

in the soil above M1 suffering from more heave, as indicated by Fig. 15. The RVE at point S0 also shows a compaction/extension-dominated deformation pattern, but different from M0, the compaction is along the X-direction as a result of surface extension caused by ground heave. The deformed RVE shows a significant change in contact normal orientation from an isotropic distribution to a Y-direction-dominated one. The RVE at point S1 suffers from not only compaction and simple shear but also large rotations. The rose diagram of contact normal orientation at point S1 shows an obvious principal axis rotation. Overall, these mesoscopic RVE responses offer a two-way verification and explanation of the global responses. This indicates that the multiscale method is

a robust and promising approach for modeling granular material in freeze-thaw loadings.

8. Closure

We have proposed a hierarchical multiscale method for simulating the freeze-thaw behavior of ice-bonded granular soils by coupling the single-point multiphase material point method (MPM) and the bond-based discrete element method (DEM). The developed semi-implicit MPM models the macroscopic thermo-hydro-mechanical responses of

freezing and thawing granular media with excellent stability and efficiency. The DEM simulation in the representative volume element (RVE) embedded in each material point provides the constitutive relationship of soils in the frozen and unfrozen states, including the bonding effect of ice between soil grains characterized by an ice saturation-dependent bond contact model. The proposed multiscale method avoids the use of conventional constitutive models for frozen/unfrozen soils by employing the contact-based grain-scale DEM simulations, which offer rich and realistic microscale details such as ice bond formation, melting and breakage.

The proposed multiscale method has been benchmarked by a 1D non-isothermal consolidation problem and a 2D cyclic cooling and heating problem before being used to simulate a boundary value problem involving freeze-thaw cycles. The detailed macroscopic and microscopic analyses demonstrate that the proposed multiscale method can capture reasonable deformation patterns, pore pressure evolutions, and stress-strain relations of soils during freeze-thaw loadings. Parallel simulations for soils with varying ice bond strengths show the significant effect of ice bonding on the global THM responses. The method is readily applicable for simulating a wide range of engineering problems in cold regions, such as frost heave or thaw settlement of foundations in changing thermal regimes and climate warming-driven landslides. Furthermore, the method can potentially be used to simulate submarine hydrate-bearing soils by considering the gas phase. Future work may integrate more elegant DEM models, such as the parallel bond contact model and the model using two sets of particles for ice and soil grains, into the current framework to facilitate more realistic modeling. In summary, the proposed approach provides a powerful alternative tool for predicting thermal-related and climate-driven granular behaviors in engineering settings.

CRediT authorship contribution statement

Jidu Yu: Writing – original draft, Methodology, Software, Validation, Investigation, Visualization, Formal analysis, Data curation, Conceptualization. **Jidong Zhao:** Writing – review & editing, Supervision, Methodology, Project administration, Funding acquisition, Investigation, Formal analysis, Conceptualization. **Weijian Liang:** Writing – review & editing, Methodology, Software, Investigation, Visualization, Formal analysis. **Shiwei Zhao:** Writing – review & editing, Methodology, Investigation, Formal analysis, Conceptualization.

Declaration of competing interest

The authors declare that they have no known competing financial interests or personal relationships that could have appeared to influence the work reported in this paper.

Data availability

Data will be made available on request.

Acknowledgments

This work is financially supported by National Natural Science Foundation of China (Project No. 11972030), Research Grants Council of Hong Kong (GRF #16207319, #16208720, #16211221, and #16206322, F-HKUST601/19, CRF #C7082-22G, TRS #T22-606/23-R), and Hetao Shenzhen-Hong Kong Science and Technology Innovation Cooperation Zone (Project #HZQBKCZYB2020083).

References

- Andersland, O.B., Ladanyi, B., 2004. Frozen ground engineering. In: *Frozen Ground Engineering*. (Ed.2), John Wiley & Sons, Inc..
- Armstrong, L., Lacelle, D., Fraser, R.H., Kokelj, S., Knudby, A., 2018. Thaw slump activity measured using stationary cameras in time-lapse and structure-from-motion photogrammetry. *Arctic Sci.* 4 (4), 827–845. <http://dx.doi.org/10.1139/as-2018-0016>.
- Arzanfudi, M.M., Al-Khoury, R., 2018. Freezing-thawing of porous media: An extended finite element approach for soil freezing and thawing. *Adv. Water Resour.* 119, 210–226. <http://dx.doi.org/10.1016/j.advwatres.2018.07.013>.
- Bai, B., 2006. Fluctuation responses of saturated porous media subjected to cyclic thermal loading. *Comput. Geotech.* 33 (8), 396–403. <http://dx.doi.org/10.1016/j.compgeo.2006.08.005>.
- Bentil, O.T., Zhou, C., 2022. Effects of temperature and thermal cycles on the elastic shear modulus of saturated clay. *J. Geotech. Geoenviron. Eng.* 148 (7), 06022006. [http://dx.doi.org/10.1061/\(ASCE\)GT.1943-5606.0002822](http://dx.doi.org/10.1061/(ASCE)GT.1943-5606.0002822).
- Chang, D., Yan, Y., Liu, J., Xu, A., Feng, L., Zhang, M., 2023. Micro-macroscopic mechanical behavior of frozen sand based on a large-scale direct shear test. *Comput. Geotech.* 159, 105484. <http://dx.doi.org/10.1016/j.compgeo.2023.105484>.
- Costard, F., Dupeyrat, L., Séjourné, A., Bouchard, F., Fedorov, A., Saint-Bézar, B., 2021. Retrogressive thaw slumps on ice-rich permafrost under degradation: Results from a large-scale laboratory simulation. *Geophys. Res. Lett.* 48 (1), e2020GL091070. <http://dx.doi.org/10.1029/2020GL091070>.
- Cui, W., Potts, D.M., Zdravković, L., Gawecka, K.A., Taborda, D.M., 2018. An alternative coupled thermo-hydro-mechanical finite element formulation for fully saturated soils. *Comput. Geotech.* 94, 22–30. <http://dx.doi.org/10.1016/j.compgeo.2017.08.011>.
- Di Donna, A., Laloui, L., 2015. Response of soil subjected to thermal cyclic loading: Experimental and constitutive study. *Eng. Geol.* 190, 65–76. <http://dx.doi.org/10.1016/j.enggeo.2015.03.003>.
- Ehlers, W., 2002. Foundations of multiphase and porous materials. In: Ehlers, W., Bluhm, J. (Eds.), *Porous Media: Theory, Experiments and Numerical Applications*. Springer, Berlin, Heidelberg, pp. 3–86. http://dx.doi.org/10.1007/978-3-662-04999-0_1.
- Eigenbrod, K.D., Knutsson, S., Sheng, D., 1996. Pore-water pressures in freezing and thawing fine-grained soils. *J. Cold Reg. Eng.* 10 (2), 77–92. [http://dx.doi.org/10.1061/\(ASCE\)0887-381X\(1996\)10:2\(77\)](http://dx.doi.org/10.1061/(ASCE)0887-381X(1996)10:2(77)).
- Evans, S.G., Ge, S., 2017. Contrasting hydrogeologic responses to warming in permafrost and seasonally frozen ground hillslopes. *Geophys. Res. Lett.* 44 (4), 1803–1813. <http://dx.doi.org/10.1002/2016GL072009>.
- Feng, K., Huang, D., Wang, G., Jin, F., Chen, Z., 2022. Physics-based large-deformation analysis of coseismic landslides: A multiscale 3D SEM-MPM framework with application to the Hongshiyuan landslide. *Eng. Geol.* 297, 106487. <http://dx.doi.org/10.1016/j.enggeo.2021.106487>.
- Feng, K., Wang, G., Huang, D., Jin, F., 2021. Material point method for large-deformation modeling of coseismic landslide and liquefaction-induced dam failure. *Soil Dyn. Earthq. Eng.* 150, 106907. <http://dx.doi.org/10.1016/j.soildyn.2021.106907>.
- Guo, N., Zhao, J., 2014. A coupled FEM/DEM approach for hierarchical multiscale modelling of granular media. *Internat. J. Numer. Methods Engrg.* 99 (11), 789–818. <http://dx.doi.org/10.1002/nme.4702>.
- Guo, N., Zhao, J., 2016. Parallel hierarchical multiscale modelling of hydro-mechanical problems for saturated granular soils. *Comput. Methods Appl. Mech. Engrg.* 305, 37–61. <http://dx.doi.org/10.1016/j.cma.2016.03.004>.
- Harris, C., Smith, J.S., Davies, M.C.R., Rea, B., 2008. An investigation of periglacial slope stability in relation to soil properties based on physical modelling in the geotechnical centrifuge. *Geomorphology* 93 (3), 437–459. <http://dx.doi.org/10.1016/j.geomorph.2007.03.009>.
- Hjort, J., Streletskiy, D., Doré, G., Wu, Q., Bjella, K., Luoto, M., 2022. Impacts of permafrost degradation on infrastructure. *Nat. Rev. Earth Environ.* 3 (1), 24–38. <http://dx.doi.org/10.1038/s43017-021-00247-8>.
- Konrad, J.M., 1989. Physical processes during freeze-thaw cycles in clayey silts. *Cold Reg. Sci. & Technol.* 16 (3), 291–303. [http://dx.doi.org/10.1016/0165-232X\(89\)90029-3](http://dx.doi.org/10.1016/0165-232X(89)90029-3).
- Kularathna, S., Liang, W., Zhao, T., Chandra, B., Zhao, J., Soga, K., 2021. A semi-implicit material point method based on fractional-step method for saturated soil. *Int. J. Numer. Anal. Methods Geomech.* 45 (10), 1405–1436. <http://dx.doi.org/10.1002/nag.3207>.
- Kurylyk, B.L., Watanabe, K., 2013. The mathematical representation of freezing and thawing processes in variably-saturated, non-deformable soils. *Adv. Water Resour.* 60, 160–177. <http://dx.doi.org/10.1016/j.advwatres.2013.07.016>.
- Lai, Y., Xu, X., Dong, Y., Li, S., 2013. Present situation and prospect of mechanical research on frozen soils in China. *Cold Reg. Sci. & Technol.* 87, 6–18. <http://dx.doi.org/10.1016/j.coldregions.2012.12.001>.
- Lei, X., He, S., Abed, A., Chen, X., Yang, Z., Wu, Y., 2021. A generalized interpolation material point method for modelling coupled thermo-hydro-mechanical problems. *Comput. Methods Appl. Mech. Engrg.* 386, 114080. <http://dx.doi.org/10.1016/j.cma.2021.114080>.

- Lewis, R.W., Majorana, C.E., Schrefler, B.A., 1986. A coupled finite element model for the consolidation of nonisothermal elastoplastic porous media. *Transp. Porous Media* 1 (2), 155–178. <http://dx.doi.org/10.1007/BF00714690>.
- Lewis, R.W., Schrefler, B.A., 1998. *The Finite Element Method in the Static and Dynamic Deformation and Consolidation of Porous Media*. John Wiley & Sons.
- Lewkowicz, A.G., Way, R.G., 2019. Extremes of summer climate trigger thousands of thermokarst landslides in a high arctic environment. *Nature Commun.* 10 (1), 1329. <http://dx.doi.org/10.1038/s41467-019-09314-7>.
- Liang, W., Wu, H., Zhao, S., Zhou, W., Zhao, J., 2022. Scalable three-dimensional hybrid continuum-discrete multiscale modeling of granular media. *Internat. J. Numer. Methods Engrg.* 123 (12), 2872–2893. <http://dx.doi.org/10.1002/nme.6963>.
- Liang, W., Zhao, J., 2019. Multiscale modeling of large deformation in geomechanics. *Int. J. Numer. Anal. Methods Geomech.* 43 (5), 1080–1114. <http://dx.doi.org/10.1002/nag.2921>.
- Liang, W., Zhao, J., Wu, H., Soga, K., 2021a. Multiscale modeling of anchor pullout in sand. *J. Geotech. Geoenviron. Eng.* 147 (9), 04021091. [http://dx.doi.org/10.1061/\(ASCE\)GT.1943-5606.0002599](http://dx.doi.org/10.1061/(ASCE)GT.1943-5606.0002599).
- Liang, W., Zhao, J., Wu, H., Soga, K., 2023. Multiscale, multiphysics modeling of saturated granular materials in large deformation. *Comput. Methods Appl. Mech. Engrg.* 405, 115871. <http://dx.doi.org/10.1016/j.cma.2022.115871>.
- Liang, W., Zhao, S., Wu, H., Zhao, J., 2021b. Bearing capacity and failure of footing on anisotropic soil: A multiscale perspective. *Comput. Geotech.* 137, 104279. <http://dx.doi.org/10.1016/j.compgeo.2021.104279>.
- Liew, M., Ji, X., Xiao, M., Farquharson, L., Nicolsky, D., Romanovsky, V., Bray, M., Zhang, X., McComb, C., 2022. Synthesis of physical processes of permafrost degradation and geophysical and geomechanical properties of permafrost. *Cold Reg. Sci. & Technol.* 198, 103522. <http://dx.doi.org/10.1016/j.coldregions.2022.103522>.
- Liu, Y., Li, K.-Q., Li, D.-Q., Tang, X.-S., Gu, S.-X., 2022. Coupled thermal-hydraulic modeling of artificial ground freezing with uncertainties in pipe inclination and thermal conductivity. *Acta Geotech.* 17 (1), 257–274. <http://dx.doi.org/10.1007/s11440-021-01221-w>.
- Liu, Z., Liu, J., Li, X., Fang, J., 2019. Experimental study on the volume and strength change of an unsaturated silty clay upon freezing. *Cold Reg. Sci. & Technol.* 157, 1–12. <http://dx.doi.org/10.1016/j.coldregions.2018.09.008>.
- Luo, J., Niu, F., Lin, Z., Liu, M., Yin, G., Gao, Z., 2022. Inventory and frequency of retrogressive thaw slumps in permafrost region of the Qinghai-Tibet Plateau. *Geophys. Res. Lett.* 49 (23), e2022GL099829. <http://dx.doi.org/10.1029/2022GL099829>.
- Ma, B., Teng, J., Li, H., Zhang, S., Cai, G., Sheng, D., 2022. A new strength criterion for frozen soil considering pore ice content. *Int. J. Geomech.* 22 (7), 04022107. [http://dx.doi.org/10.1061/\(ASCE\)GM.1943-5622.0002433](http://dx.doi.org/10.1061/(ASCE)GM.1943-5622.0002433).
- Ma, W., Zhang, L., Yang, C., 2015. Discussion of the applicability of the generalized Clausius-Clapeyron equation and the frozen fringe process. *Earth-Sci. Rev.* 142, 47–59. <http://dx.doi.org/10.1016/j.earscirev.2015.01.003>.
- McTigue, D.F., 1986. Thermoelastic response of fluid-saturated porous rock. *J. Geophys. Res.* 91 (B9), 9533. <http://dx.doi.org/10.1029/JB091iB09p09533>.
- Na, S., Sun, W., 2017. Computational thermo-hydro-mechanics for multiphase freezing and thawing porous media in the finite deformation range. *Comput. Methods Appl. Mech. Engrg.* 318, 667–700. <http://dx.doi.org/10.1016/j.cma.2017.01.028>.
- Neaupane, K.M., Yamabe, T., Yoshinaka, R., 1999. Simulation of a fully coupled thermo-hydro-mechanical system in freezing and thawing rock. *Int. J. Rock Mech. Min. Sci.* 36 (5), 563–580. [http://dx.doi.org/10.1016/S0148-9062\(99\)00026-1](http://dx.doi.org/10.1016/S0148-9062(99)00026-1).
- Ng, C.W.W., Wang, S.H., Zhou, C., 2016. Volume change behaviour of saturated sand under thermal cycles. *Géotech. Lett.* 6 (2), 124–131. <http://dx.doi.org/10.1680/jgele.15.00148>.
- Nicot, F., Hadda, N., Guessasma, M., Fortin, J., Millet, O., 2013. On the definition of the stress tensor in granular media. *Int. J. Solids Struct.* 50 (14), 2508–2517. <http://dx.doi.org/10.1016/j.ijsolstr.2013.04.001>.
- Nishimura, S., Gens, A., Olivella, S., Jardine, R.J., 2009. THM-coupled finite element analysis of frozen soil: Formulation and application. *Géotechnique* 59 (3), 159–171. <http://dx.doi.org/10.1680/geot.2009.59.3.159>.
- Nishimura, S., Okajima, S., Joshi, B.R., Higo, Y., Tokoro, T., 2021. Volumetric behaviour of clays under freeze-thaw cycles in a mesoscopically uniform element. *Géotechnique* 71 (12), 1150–1164. <http://dx.doi.org/10.1680/jgeot.20.P.047>.
- Niu, F., Luo, J., Lin, Z., Fang, J., Liu, M., 2016. Thaw-induced slope failures and stability analyses in permafrost regions of the Qinghai-Tibet Plateau, China. *Landslides* 13 (1), 55–65. <http://dx.doi.org/10.1007/s10346-014-0545-2>.
- Noorishad, J., Tsang, C.F., Witherspoon, P.A., 1984. Coupled thermal-hydraulic-mechanical phenomena in saturated fractured porous rocks: Numerical approach. *J. Geophys. Res.: Solid Earth* 89 (B12), 10365–10373. <http://dx.doi.org/10.1029/JB089iB12p10365>.
- Qi, J., Ma, W., Song, C., 2008. Influence of freeze-thaw on engineering properties of a silty soil. *Cold Reg. Sci. & Technol.* 53 (3), 397–404. <http://dx.doi.org/10.1016/j.coldregions.2007.05.010>.
- Qi, J., Vermeer, P.A., Cheng, G., 2006. A review of the influence of freeze-thaw cycles on soil geotechnical properties. *Permafrost Periglac. Process.* 17 (3), 245–252. <http://dx.doi.org/10.1002/ppp.559>.
- Schuur, E.A.G., McGuire, A.D., Schädel, C., Grosse, G., Harden, J.W., Hayes, D.J., Hugelius, G., Koven, C.D., Kuhry, P., Lawrence, D.M., Natali, S.M., Olefeldt, D., Romanovsky, V.E., Schaefer, K., Turetsky, M.R., Treat, C.C., Vonk, J.E., 2015. Climate change and the permafrost carbon feedback. *Nature* 520 (7546), 171–179. <http://dx.doi.org/10.1038/nature14338>.
- Shastri, A., Sánchez, M., Gai, X., Lee, M.Y., Dewers, T., 2021. Mechanical behavior of frozen soils: Experimental investigation and numerical modeling. *Comput. Geotech.* 138, 104361. <http://dx.doi.org/10.1016/j.compgeo.2021.104361>.
- Shen, C.-M., Yu, J.-D., Liu, S.-H., Mao, H.-Y., 2021. A unified fractional breakage model for granular materials inspired by the crushing tests of dyed gypsum particles. *Constr. Build. Mater.* 270, 121366. <http://dx.doi.org/10.1016/j.conbuildmat.2020.121366>.
- Suh, H.S., Sun, W., 2022. Multi-phase-field microporomechanics model for simulating ice-lens growth in frozen soil. *Int. J. Numer. Anal. Methods Geomech.* 46 (12), 2307–2336. <http://dx.doi.org/10.1002/nag.3408>.
- Sun, R., Liu, R., Zhang, H., Liu, C., Li, C., 2023. DEM investigation of the mechanical behavior of frozen soil along various stress paths. *Bull. Eng. Geol. Environ.* 82 (9), 351. <http://dx.doi.org/10.1007/s10064-023-03367-1>.
- Sweidan, A.H., Heider, Y., Markert, B., 2020. A unified water/ice kinematics approach for phase-field thermo-hydro-mechanical modeling of frost action in porous media. *Comput. Methods Appl. Mech. Engrg.* 372, 113358. <http://dx.doi.org/10.1016/j.cma.2020.113358>.
- Ting, Z., Li, D., East, A., Walling, D., Lane, S., Overeem, I., Beylich, A., Koppes, M., Lu, X.X., 2022. Warming-driven erosion and sediment transport in cold regions. *Nat. Rev. Earth Environ.* 3, <http://dx.doi.org/10.1038/s43017-022-00362-0>.
- Tounsi, H., Rouabhi, A., Tijani, M., Guérin, F., 2019. Thermo-Hydro-Mechanical Modeling of Artificial Ground Freezing: Application in Mining Engineering. *Rock Mech. Rock Eng.* 52 (10), 3889–3907. <http://dx.doi.org/10.1007/s00603-019-01786-9>.
- Turetsky, M.R., Abbott, B.W., Jones, M.C., Walter Anthony, K., Olefeldt, D., Schuur, E.A.G., Koven, C., McGuire, A.D., Grosse, G., Kuhry, P., Hugelius, G., Lawrence, D.M., Gibson, C., Sannel, A.B.K., 2019. Permafrost collapse is accelerating carbon release. *Nature* 569 (7754), 32–34. <http://dx.doi.org/10.1038/d41586-019-01313-4>.
- van Genuchten, M.T., 1980. A closed-form equation for predicting the hydraulic conductivity of unsaturated soils. *Soil Sci. Am. J.* 44 (5), 892–898. <http://dx.doi.org/10.2136/sssaj1980.03615995004400050002x>.
- Viklander, P., 1998. Permeability and volume changes in till due to cyclic freeze/thaw. *Can. Geotech. J.* 35 (3), 471–477. <http://dx.doi.org/10.1139/t98-015>.
- Wang, P., Liu, E., Zhi, B., Song, B., Yu, Q., Wang, J., Sun, R., 2024. A macro-meso nonlinear strength criterion for frozen soil. *Acta Geotech.* <http://dx.doi.org/10.1007/s11440-023-02197-5>.
- Wang, D.-y., Ma, W., Wen, Z., Chang, X.-x., 2008. Study on strength of artificially frozen soils in deep alluvium. *Tunnel. Undergr. Space Technol.* 23 (4), 381–388. <http://dx.doi.org/10.1016/j.tust.2007.06.010>.
- Wang, B., Paudel, B., Li, H., 2016. Behaviour of retrogressive thaw slumps in northern Canada—three-year monitoring results from 18 sites. *Landslides* 13 (1), 1–8. <http://dx.doi.org/10.1007/s10346-014-0549-y>.
- Wang, T., Yang, D., Yang, Y., Piao, S., Li, X., Cheng, G., Fu, B., 2020. Permafrost thawing puts the frozen carbon at risk over the Tibetan Plateau. *Sci. Adv.* 6 (19), eaz3513. <http://dx.doi.org/10.1126/sciadv.aaz3513>.
- Wu, R., 2008. *Analytical Study on One-Dimensional Thermal Consolidation Theory of Saturated Soil* (Ph.D. thesis). Zhejiang University.
- Wu, H., Guo, N., Zhao, J., 2018a. Multiscale modeling and analysis of compaction bands in high-porosity sandstones. *Acta Geotech.* 13 (3), 575–599. <http://dx.doi.org/10.1007/s11440-017-0560-2>.
- Wu, H., Papazoglou, A., Viggiani, G., Dano, C., Zhao, J., 2020. Compaction bands in Tuffeau de Maastricht: Insights from X-ray tomography and multiscale modeling. *Acta Geotech.* 15 (1), 39–55. <http://dx.doi.org/10.1007/s11440-019-00904-9>.
- Wu, H., Zhao, J., Guo, N., 2018b. Multiscale insights into borehole instabilities in high-porosity sandstones. *J. Geophys. Res.: Solid Earth* 123 (5), 3450–3473. <http://dx.doi.org/10.1029/2017JB015366>.
- Xu, X., Lai, Y., Dong, Y., Qi, J., 2011. Laboratory investigation on strength and deformation characteristics of ice-saturated frozen sandy soil. *Cold Reg. Sci. & Technol.* 69 (1), 98–104. <http://dx.doi.org/10.1016/j.coldregions.2011.07.005>.
- Xu, X., Wang, B., Fan, C., Zhang, W., 2020. Strength and deformation characteristics of silty clay under frozen and unfrozen states. *Cold Reg. Sci. & Technol.* 172, 102982. <http://dx.doi.org/10.1016/j.coldregions.2019.102982>.
- Yang, Y., Lai, Y., Chang, X., 2010. Laboratory and theoretical investigations on the deformation and strength behaviors of artificial frozen soil. *Cold Reg. Sci. & Technol.* 64 (1), 39–45. <http://dx.doi.org/10.1016/j.coldregions.2010.07.003>.
- Yu, J., Shen, C., Liu, S., Cheng, Y.P., 2020. Exploration of the survival probability and shape evolution of crushable particles during one-dimensional compression using dyed gypsum particles. *J. Geotech. Geoenviron. Eng.* 146 (11), 04020121. [http://dx.doi.org/10.1061/\(ASCE\)GT.1943-5606.0002371](http://dx.doi.org/10.1061/(ASCE)GT.1943-5606.0002371).
- Yu, J., Zhao, J., Liang, W., Zhao, S., 2024a. A semi-implicit material point method for coupled thermo-hydro-mechanical simulation of saturated porous media in large deformation. *Comput. Methods Appl. Mech. Engrg.* 418, 116462. <http://dx.doi.org/10.1016/j.cma.2023.116462>.
- Yu, J., Zhao, J., Zhao, S., Liang, W., 2024b. Multiphysics modeling of freeze-thaw behavior of porous media in large deformation. *Int. J. Numer. Anal. Methods Geomech.* under review.

- Yuan, W.-H., Zheng, H., Zheng, X., Wang, B., Zhang, W., 2023. An improved semi-implicit material point method for simulating large deformation problems in saturated geomaterials. *Comput. Geotech.* 161, 105614. <http://dx.doi.org/10.1016/j.compgeo.2023.105614>.
- Yuan, W.-H., Zhu, J.-X., Liu, K., Zhang, W., Dai, B.-B., Wang, Y., 2022. Dynamic analysis of large deformation problems in saturated porous media by smoothed particle finite element method. *Comput. Methods Appl. Mech. Engrg.* 392, 114724. <http://dx.doi.org/10.1016/j.cma.2022.114724>.
- Zhang, Y., Carey, S.K., Quinton, W.L., 2008. Evaluation of the algorithms and parameterizations for ground thawing and freezing simulation in permafrost regions. *J. Geophys. Res.: Atmos.* 113 (D17), <http://dx.doi.org/10.1029/2007JD009343>.
- Zhang, D., Liu, E., Liu, X., Zhang, G., Song, B., 2017. A new strength criterion for frozen soils considering the influence of temperature and coarse-grained contents. *Cold Reg. Sci. & Technol.* 143, 1–12. <http://dx.doi.org/10.1016/j.coldregions.2017.08.006>.
- Zhang, L., Ma, W., Yang, C., 2015. Pore water pressure changes of supercooling and ice nucleation stages during freezing point testing. *Géotech. Lett.* 5 (1), 39–42. <http://dx.doi.org/10.1680/geolett.14.00109>.
- Zhang, L., Ma, W., Yang, C., Wen, Z., Dong, S., 2016. An investigation of pore water pressure and consolidation phenomenon in the unfrozen zone during soil freezing. *Cold Reg. Sci. & Technol.* 130, 21–32. <http://dx.doi.org/10.1016/j.coldregions.2016.07.007>.
- Zhang, L., Ma, W., Yang, C., Yuan, C., 2014. Investigation of the pore water pressures of coarse-grained sandy soil during open-system step-freezing and thawing tests. *Eng. Geol.* 181, 233–248. <http://dx.doi.org/10.1016/j.enggeo.2014.07.020>.
- Zhang, M., Zhang, X., Lai, Y., Lu, J., Wang, C., 2020. Variations of the temperatures and volumetric unfrozen water contents of fine-grained soils during a freezing–thawing process. *Acta Geotech.* 15 (3), 595–601. <http://dx.doi.org/10.1007/s11440-018-0720-z>.
- Zhao, S., Chen, H., Zhao, J., 2022a. Multiscale modeling of freeze-thaw behavior in granular media. *Acta Mech. Sin.* 39 (1), 722195. <http://dx.doi.org/10.1007/s10409-022-22195-x>.
- Zhao, S., Zhao, J., Lai, Y., 2020. Multiscale modeling of thermo-mechanical responses of granular materials: A hierarchical continuum–discrete coupling approach. *Comput. Methods Appl. Mech. Engrg.* 367, 113100. <http://dx.doi.org/10.1016/j.cma.2020.113100>.
- Zhao, S., Zhao, J., Liang, W., Niu, F., 2022b. Multiscale modeling of coupled thermo-mechanical behavior of granular media in large deformation and flow. *Comput. Geotech.* 149, 104855. <http://dx.doi.org/10.1016/j.compgeo.2022.104855>.
- Zhou, Z., Ma, W., Zhang, S., Mu, Y., Li, G., 2018. Effect of freeze-thaw cycles in mechanical behaviors of frozen loess. *Cold Reg. Sci. & Technol.* 146, 9–18. <http://dx.doi.org/10.1016/j.coldregions.2017.11.011>.
- Zhou, M., Meschke, G., 2013. A three-phase thermo-hydro-mechanical finite element model for freezing soils. *Int. J. Numer. Anal. Methods Geomech.* 37 (18), 3173–3193. <http://dx.doi.org/10.1002/nag.2184>.
- Zhu, T., Chen, J., Huang, D., Luo, Y., Li, Y., Xu, L., 2021. A DEM-based approach for modeling the damage of rock under freeze–thaw cycles. *Rock Mech. Rock Eng.* 54 (6), 2843–2858. <http://dx.doi.org/10.1007/s00603-021-02465-4>.